







Dynamics of a buffer-gas-loaded, deep optical trap for molecules

Ashwin Singh ^{*}, Lothar Maisenbacher , Ziguang Lin , Jeremy J. Axelrod [†], Cristian D. Panda , and Holger Müller 
Department of Physics, University of California, Berkeley, Berkeley, California 94720, USA

 (Received 9 February 2023; accepted 24 May 2023; published 5 July 2023)

We describe an approach to optically trapping small, chemically stable molecules at cryogenic temperatures by buffer-gas loading a deep optical dipole trap. The ~ 10 K trap depth will be produced by a tightly focused, 1064-nm cavity capable of reaching intensities of hundreds of GW/cm². Molecules will be directly buffer-gas loaded into the trap using a helium buffer gas at 1.5 K. The very far-off-resonant, quasielectrostatic trapping mechanism is insensitive to a molecule's internal state, energy level structure, and its electric and magnetic dipole moment. Here, we theoretically investigate the trapping and loading dynamics, as well as the heating and loss rates, and conclude that 10^4 – 10^6 molecules are likely to be trapped. Our trap would open new possibilities in molecular spectroscopy, studies of cold chemical reactions, and precision measurement, amongst other fields of physics.

DOI: [10.1103/PhysRevResearch.5.033008](https://doi.org/10.1103/PhysRevResearch.5.033008)

I. INTRODUCTION

A. Background

Cooling and trapping of atoms and ions has enabled unparalleled quantum control of both internal and external degrees of freedom [1]. It has led to advances in quantum information processing [2], quantum simulation [3], studies of cold phases of matter [4], spectroscopy and atomic clocks [5], and tests of the Standard model [6], amongst other areas of physics. Molecules possess a rich internal energy level structure not seen in atoms, consisting of rotational and vibrational transitions in addition to electronic transitions. This complexity has generated great interest in cooling and trapping molecules [7,8]. Trapped polar molecules have been proposed as potential qubits for quantum information processing [9], with the possibility of using their rotational states for quantum error correction [10]. Cold, trapped molecules can exhibit unique phases of matter [11–13], and large polar molecules have applications in tests of Standard Model physics [14–16]. Furthermore, there is much interest in studying the cold chemistry of trapped molecules [11,17–19]. For this reason, it is a goal of atomic, molecular and optical physics to develop a trap for arbitrary chemical species.

In recent decades, significant progress has been made towards this ambitious goal. Crossed or merged molecular beams have become established techniques used to interrogate cold collisions over short interaction times [20–22].

Buffer-gas cooling has enabled the production of a broad spectrum of molecular samples at temperatures of order 1 K [23], which has allowed for cold spectroscopic experiments [24,25], as well as trapping low-field-seeking paramagnetic molecules in magnetic traps [26–28] and molecular ions in ion traps [29,30]. Polar molecules like ND₃ [31], OH [32], CH₃F [32], and CH₂O [33] have been loaded from low-field-seeking states in buffer-gas beams into low-density electrostatic traps. It has been proposed that polar molecules in their true, high-field seeking ground state could be deeply trapped in an intense microwave trap addressing rotational transitions in the molecules [34], and progress has been made on trapping ultracold atoms in this kind of trap [35]. Other molecules, particularly alkalis, have been trapped through photoassociation of ultracold atoms in optical traps [36–38]. For a limited number of molecules, with a bivalent metal connected to a ligand to produce an “alkali-like” energy structure [39–47], laser cooling has been achieved, albeit requiring multiple repump lasers addressing loss channels into other rovibrational states [48].

Unfortunately, none of these techniques is universally applicable, and access to cold molecules remains limited. Magnetic and electrostatic traps are limited to molecules with a large magnetic or electric dipole moment, respectively, and only trap molecules in excited, low-field-seeking states, which leads to loss through state-changing collisions. Optical dipole traps (ODTs), based on the attractive force of an infrared laser beam, are now widely used. Still, even with hundreds of watts of laser power, they are limited to mK trap depths, and thus to the few species of molecules that have been laser-cooled.

B. Buffer-gas-loaded dipole trap

Here, we consider trapping neutral molecules in their ground state with a deep optical dipole trap, taking an additional step towards the ultimate goal of a universal trap. Our proposed design is shown in Fig. 1. This trap, originally

^{*}ashwin_singh@berkeley.edu

[†]Also at Lawrence Berkeley National Laboratory, Berkeley, CA 94720, USA.

Published by the American Physical Society under the terms of the Creative Commons Attribution 4.0 International license. Further distribution of this work must maintain attribution to the author(s) and the published article's title, journal citation, and DOI.

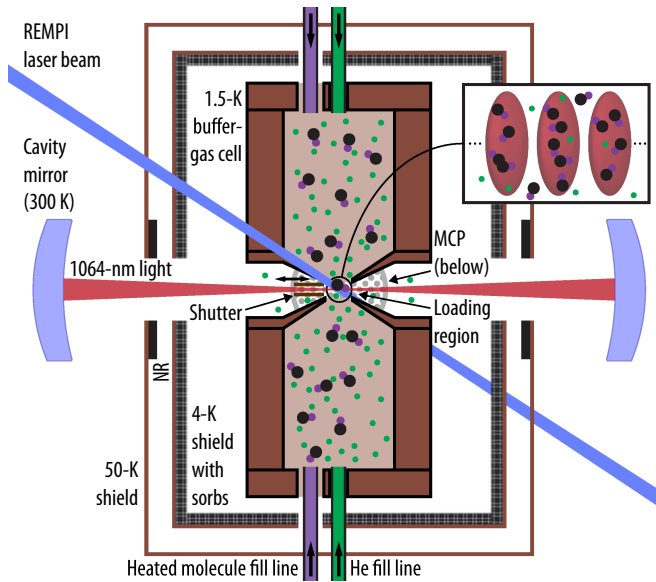


FIG. 1. Schematic design of the buffer-gas-loaded, deep optical trap for molecules. The optical trap is formed by 1064-nm light (red beam) inside a 100-mm-long, near-concentric build-up cavity, whose mirrors are held at room temperature. Helium buffer gas (He; shown in green) at 1.5 K and molecules (black and purple) at a higher temperature flow through fill lines into two opposing cryogenic cells, held at 1.5 K. The molecules thermalize with the buffer gas and flow, along with the buffer gas, through conical apertures into the loading region. Here, the molecules are loaded through buffer-gas collisions into, and subsequently trapped in, the distinct lattice sites formed by the antinodes of the standing wave of the cavity (inset on top right). Shutters in front of the cells can quickly interrupt the flow out of the cells to create an isolated sample of trapped molecules. Resonance-enhanced multiphoton ionization (REMPI) with a second laser beam (blue beam) ionizes the molecules, which are then detected with a microchannel plate (MCP). Also shown are radiation shields at 50 and 4 K (with attached charcoal sorbs used for cryopumping of He), and nonreflective (NR) material to absorb scattered light. The drawing is to scale.

envisioned decades ago [49], is made possible by the development of high-intensity cavities able to generate continuous-wave (CW) laser intensities over 400 GW/cm^2 with 1064-nm light [50–52]. At such high intensities, a very far-off-resonant, quasioleostatic dipole trap has a trap depth of order 10 K for most molecules. Buffer-gas cooling with ^4He in the trap volume is therefore sufficient to load molecules into the trap. After equilibration, the buffer gas is pumped out of the chamber, leaving a trapped sample in the laser beam. These methods rely only on a molecule’s DC polarizability, which is nonzero for any species, and do not require a particular energy level structure or magnetic or polar molecules. This not only allows a large number of species that cannot be trapped by existing methods to be loaded into our dipole trap, but also for two or more different species to be trapped at the same time.

Although our methods should be applicable to molecules of any symmetry, we will limit ourselves to discussing linear molecules for simplicity. Table I summarizes our results. Molecules with typical mean DC polarizabilities ($\alpha_s \lesssim 2 \text{ \AA}^3$, averaged over all orientations), high ionization ener-

gies ($I_0 \sim 12 \text{ eV}$), few atoms (≤ 3), and low DC polarizability anisotropies ($\Delta\alpha_s \lesssim 1 \text{ \AA}^3$) are good candidates for our trap, but other molecules could be trapped with small modifications to the trap design. With so many molecules to consider, for clarity we will frequently refer to a hypothetical molecule Q as a representative of molecules we wish to trap. Q is a small, chemically stable (SCS) molecule with characteristics similar to many of the molecules in Table I. We choose the polarizability and ionization energy of Q to be $\alpha_s = 2 \text{ \AA}^3$ and $I_0 = 12 \text{ eV}$, respectively, based on the species listed in Table I. Furthermore, we assume Q ’s polarizability to be isotropic (i.e., zero $\Delta\alpha_s$), and take Q to have a boiling point of $T_B = 200 \text{ K}$ and a molecular mass of $m_Q = 30 \text{ u}$. These are typical values for SCS molecules, and we note that the trapping is not sensitive to the exact values.

C. Outline

The experimental design, including the cavity and the buffer-gas cells, is discussed in Sec. II. Section III treats the very far-off-resonant, quasioleostatic dipole trapping of molecules. Section IV considers the effects of the high-intensity light on the molecules in the trap. The dynamics of buffer-gas cooling and loading into the trap are the subject of Sec. V. Finally, the ionization-based detection of molecules is reviewed in Sec. VI, and a summary and outlook are given in Sec. VII.

II. EXPERIMENTAL DESIGN

A. Near-concentric build-up cavity for 1064-nm light

The high-intensity, 1064-nm trap light is produced by a near-concentric build-up cavity, modeled on a demonstrated cavity designed by our group [50]. The demonstrated cavity has a finesse of $\mathcal{F} \approx 37000$ and a power enhancement factor $P_{\text{circ}}/P_{\text{in}} \approx 9000$ (accounting for coupling inefficiencies and technical losses). By coupling input powers $P_{\text{in}} \approx 15 \text{ W}$ into the fundamental TEM_{00} mode of the cavity, circulating powers of $P_{\text{circ}} \geq 125 \text{ kW}$ have been achieved. With the 20-mm-long, symmetric cavity operating $10 \mu\text{m}$ from concentricity, the mode has been focused to a waist of $w_0 \approx 8.7 \mu\text{m}$ ($1/e^2$ intensity radius), resulting in an intensity $\geq 400 \text{ GW/cm}^2$ at the antinodes of the cavity’s standing intensity wave [50].

Compared to Ref. [50], we require a five-fold increase in the cavity length to 100 mm, which creates space for the cryogenic system surrounding the cavity focus. To achieve the same mode waist, the longer cavity needs to be aligned closer to concentricity, which makes it more sensitive to misalignments. In particular, thermal mirror deformation from laser-induced, local heating has a tendency to increase the mode waist and hence decrease the intensity in the cavity. While a detailed analysis is beyond the scope of this work, using mirrors made from ultralow expansion glass (ULE), coated with an ultralow-absorption reflective coating [with an absorption as low as 0.4 ppm at 1064 nm (unpublished measurement by our group)], will allow us to achieve an intensity of $I = 300 \text{ GW/cm}^2$ with a mode waist of $w_0 = 8 \mu\text{m}$, based on extrapolating the data of [50,72].

TABLE I. Candidate small, chemically stable (SCS) molecules, including our hypothetical molecule Q . All molecules listed are linear symmetric tops. Entries are calculated assuming a laser intensity of $I = 300 \text{ GW/cm}^2$ at a wavelength of $\lambda = 1064 \text{ nm}$. The mean value α_s and the anisotropy $\Delta\alpha_s$ of the DC polarizability determine the trap depth T_{trap} , with ΔT_{trap} being the contribution to T_{trap} from molecular alignment by the intense trap light (see Appendix A). The Rayleigh and rotational Raman scattering rates, W_R and W_{RR} , are proportional to the square of α_s and $\Delta\alpha_s$, respectively (see Secs. IV A and IV B). The ionization energy I_0 is used to estimate the ionization rate W_i (see Sec. IV C). Additionally, the mass m and boiling point T_B are given. Resonance-enhanced multiphoton ionization (REMPI) schemes for detection of each molecule are shown (see Sec. VI), where $n + l$ refers to a scheme absorbing a total of $n + l$ photons at the given wavelength(s). Entries and relevant spectra are taken from a variety of public databases and individual publications [53–58].

Species	α_s (\AA^3)	$\Delta\alpha_s$ (\AA^3)	T_{trap} (K)	ΔT_{trap} (K)	I_0 (eV)	W_R (s^{-1})	W_{RR} (s^{-1})	W_i (s^{-1})	m (u)	T_B (K)	REMPI scheme
Suitable for cooling, trapping, and REMPI detection with the experimental parameters proposed here											
N_2	1.7	0.7	7.8	0.1	15.6	479	17	1.6×10^{-18}	28	77	2+2, 283 nm [59] ^c
CO	2.0	0.5	8.9	0.0	14.0	624	10	3.7×10^{-15}	28	82	2+1, 230 nm [60]
O_2	1.6	1.1	7.3	0.2	12.1	399	43	2.5×10^{-9}	32	90	2+1, 215–240 nm [61]
HCl	2.5	0.3	11.5	0.0	12.7	1035	4	3.3×10^{-10}	36	188	2+1, 208–260 nm [62]
Xe ^a	4.0	0.0	18.2	0.0	12.1	2626	0	2.2×10^{-9}	131	165	2+1, 224 nm [63]
Lower mean DC polarizability α_s , requiring higher intensity I											
H	0.7	0.0	3.0	0.0	13.6	73	0	1.1×10^{-12}	1	21	2+1, 243 nm [64]
H_2	0.8	0.3	3.6	0.0	15.4	101	4	2.0×10^{-18}	2	20	2+1, 202 nm [65]
⁴ He ^b	0.2	0.0	0.9	0.0	24.6	7	0	7.8×10^{-44}	4	4	–
Might require longer wavelength because of larger rotational Raman scattering rate W_{RR} and/or ionization rate W_i											
CO_2	2.5	2.1	13.8	2.4	13.8	1029	160	6.8×10^{-13}	44	195	3+1, 280–330 nm [66]
N_2O	3.0	3.0	17.6	3.9	12.9	1471	319	4.1×10^{-12}	44	185	1+2+1, 204 nm [67] ^d
Cl_2	4.6	2.6	25.2	4.2	11.5	3479	246	6.4×10^{-7}	70	239	2+1, 220–260 nm [68]
CS_2	8.7	9.5	63.5	23.7	10.1	12529	3255	1.2×10^{-3}	76	319	1+1, 208–217 nm [69]
NO	1.7	0.8	7.8	0.1	9.3	472	26	2.0×10^{-1}	30	121	1+1, 226 nm [70]
Hypothetical molecule Q (see text)											
Q	2.0	0.0	9.1	0.0	12.0	655	0	2.8×10^{-9}	30	200	–

^aAtomic Xe is included as its properties make it a good test species for experimental designs.

^bIncluded for reference.

^cAlso: 2+1, 202 nm [71].

^dPhotodissociation of N_2O into N_2 and O, followed by 2+1 REMPI of N_2 , using the same laser beam at 204 nm.

Our cavity mirrors will be kept outside the cryogenic system to prevent buildup of frozen molecules on their surfaces. The high intensity and high finesse of the cavity limits the use of optical elements like windows in the cavity's optical path. Therefore, as shown in Fig. 1, our cryogenic system will have apertures that let in the cavity light. To prevent diffraction losses, the diameter of these apertures is here chosen to be four times the $1/e^2$ intensity beam diameter.

B. Buffer-gas cells

A 1.5-K buffer gas is used to both cool and load the molecules into the trap. Many aspects of the design of buffer-gas cells benefit from the extensive work done in other experiments [26,27,73–75]. However, as opposed to creating a buffer-gas beam [74,75] or loading our trap within a buffer-gas cell [26,27], we here opt to populate a millimeter-scale loading region between two cells, centered on the dipole trap, with buffer gas and cold molecules. This minimizes the amount of gas pumpout required and allows for optical access. Furthermore, since our experiment is critically dependent on highly reflective cavity mirrors whose sensitivity to ablation

byproducts is unknown, we will not source molecules in the cells using laser ablation, and instead will flow molecules into the buffer-gas cells through heated fill lines. The resulting dual-buffer-gas-cell geometry is depicted in Fig. 1, and uses two closely spaced, cylindrically symmetric, opposing 1.5-K cells of ~ 30 -mm dimensions and conical apertures with a diameter of 5 mm. This design was validated to achieve the required densities and sufficient thermalization using the direct simulation Monte Carlo (DSMC) method [76]. Vacuum is maintained outside the loading region by differential pumping with activated charcoal sorbs on the 4-K shield at 6 L/s/cm^2 [77]. Pumping out the loading region is done by shutting off flow from the buffer-gas cells using rapidly actuating, cryogenic shutters. Based on the demonstrated shutter of [25], we assume a shutter can actuate in 1 ms, which sets the pumpout timescale from the loading region in our experiment.

C. Heat load on cryogenic system

The cells will be maintained at 1.5 K by thermal contact to a ⁴He-filled 1-K pot, which is pre-cooled and radiation-shielded by 4-K and 50-K stages of a pulse-tube cryocooler.

Commercially available cryocoolers are able to provide 100 mW of cooling power at 1.5 K, which sets the heat-load budget for the experiment.

The conductive heat load from the heated molecule fill lines has been shown to be manageable by previous experiments, including one using a fill line for water held at 280 K connected to a similar buffer-gas cell [78]. Convective heat loads will be managed by differential pumping with activated charcoal. Radiative heat loads on the buffer-gas cells through the apertures in the radiation shields are estimated to be less than 10 mW.

Another major heat load is scattering of the high-intensity cavity light off the mirrors through the apertures onto the buffer-gas cells. Polishing the cells to enhance their reflectivity, and carefully designing the radiation shields, including adding nonreflective (NR) material to the 50-K shields (see Fig. 1), manages this heat load (see Appendix B).

III. DIPOLE TRAPPING OF MOLECULES

A. Trap depth

Most small, chemically stable (SCS) molecules have limited activity in the optical and near-infrared (NIR) spectrum. Therefore a dipole trap using light at a wavelength of $\lambda = 1064$ nm is red-detuned by several harmonics from the first electronic transition of a typical SCS molecule. In this regime, the commonly used rotating wave approximation does not apply, and the light produces a quasielectrostatic trap by creating a dipole potential [79–82]

$$U \approx -\frac{\alpha_s}{2} \langle |\mathbf{E}|^2 \rangle = -\frac{\alpha_s}{4} E_0^2 = -\frac{\alpha_s I}{2\epsilon_0 c}, \quad (1)$$

where α_s is the mean DC polarizability [83] and $\langle \cdot \rangle$ denotes a time average over the optical period $2\pi/\omega = \lambda/c$ (ω : optical angular frequency, c : speed of light). The oscillating electric field is given by $\mathbf{E} = E_0 \cos(\omega t) \hat{\mathbf{E}}$, with $\hat{\mathbf{E}}$ the normalized polarization vector and E_0 the electric field amplitude. The intensity is $I = \epsilon_0 c \langle |\mathbf{E}|^2 \rangle = \epsilon_0 c E_0^2 / 2$ (ϵ_0 : permittivity of free space). From Eq. (1), the intensity required for a 10 K trap depth depends simply on α_s as $I|_{T_{\text{trap}}=10\text{K}} \approx (659 \text{ GW/cm}^2) / (\alpha_s [\text{\AA}^3])$.

The trap depth of several K is comparable to the rotational energy level spacing of many SCS molecules. The trap may therefore significantly hybridize the rotational levels and align the molecules' most polarizable axis with the optical polarization, leading to an increase in the trap depth that is not accounted for in Eq. (1) [49,84,85]. The trap depth $T_{\text{trap}} = \max(|U|/k_B)$ (k_B Boltzmann's constant) as listed in Table I therefore includes a correction to Eq. (1) of ΔT_{trap} , which depends on the polarizability anisotropy $\Delta\alpha_s$ and is discussed in Appendix A. This correction is usually only a few percent of T_{trap} , but for highly anisotropic molecules like CS_2 it can be substantial.

As seen in Table I, most molecules have $T_{\text{trap}} \gtrsim 10$ K at our intensity $I = 300 \text{ GW/cm}^2$, more than six times the buffer gas temperature. Species with particularly low polarizabilities, like H and H_2 , may still be trapped deeply if much higher intensities can be generated. Helium buffer gas atoms are also attracted to the trap center, but with a smaller trap depth of

$T_{\text{trap}} = 0.95$ K due to their low polarizability. We ignore this small effect in the rest of this publication.

Molecules typically have a rich spectrum of pure rovibrational transitions. Although the trap light is blue-detuned from all pure rovibrational transitions, these transitions do not contribute significantly to the dynamic polarizability at 1064 nm [86–88], and hence do not lead to antitrapping. Typical SCS molecules are in their electronic ground state and predominantly in their rovibrational ground state at our chosen buffer gas temperature of $T = 1.5$ K.

B. Optical potential

The trap itself is characterised firstly by the trap depth $T_{\text{trap}} = \max |U|/k_B$. Since our trap light is the Gaussian TEM_{00} mode of an optical cavity, the spatial dependence of the trapping potential, in cylindrical coordinates measured relative to the focus of the cavity (placed at the origin), is

$$\begin{aligned} U(r, z) &= -k_B T_{\text{trap}} \frac{e^{-2r^2/w^2(z)}}{1 + z^2/z_R^2} \\ &\times \cos^2 \left(kz + \tan^{-1} \left(\frac{z}{z_R} \right) + \frac{kr^2}{2R(z)} \right) \\ &\approx -k_B T_{\text{trap}} \frac{w_0^2}{w^2(z)} e^{-2r^2/w^2(z)} \cos^2(kz), \end{aligned} \quad (2)$$

where the approximation is valid near the focus of the trap. Here, $k = 2\pi/\lambda$, $w(z) = w_0 \sqrt{1 + z^2/z_R^2}$, $R(z) = z + z_R^2/z$, and $z_R = kw_0^2/2$ is the Rayleigh range.

Appreciable molecule loading will only occur in the region where the trap potential is large compared to the buffer gas temperature. The trap volume is therefore characterized approximately by the volume within which $U(r, z) \geq 3k_B T$, which is sensitive to the dimensionless trap depth parameter $\eta_0 = T_{\text{trap}}/T$:

$$V \approx \frac{2\pi w_0^2 z_R}{9} \left[\sqrt{\frac{\eta_0}{3} - 1} \left(\frac{\eta_0}{3} + 5 \right) - 6 \tan^{-1} \left(\sqrt{\frac{\eta_0}{3} - 1} \right) \right]. \quad (3)$$

We note that V thus scales as w_0^4 . This volume is split nonuniformly into $4\sqrt{\frac{\eta_0}{3} - 1} z_R/\lambda$ distinct lattice sites, spaced axially by $\lambda/2$.

We propose Q be loaded from a buffer gas at 1.5 K into our 1064-nm dipole trap with a peak intensity of 300 GW/cm^2 and an $8 \mu\text{m}$ waist. The resulting trap depth is 9.4 K, and $\eta_0 = 6.3$. The corresponding approximate trap volume is $V = 1.8 w_0^2 z_R = 2.2 \times 10^{-8} \text{ cm}^3$, and there are 743 distinct lattice sites with a site depth greater than $3k_B T$.

IV. EFFECTS OF HIGH-INTENSITY LIGHT ON TRAPPED MOLECULES

In this section, we review Rayleigh and Raman scattering, photoionization, and photodissociation of molecules, and determine the class of molecules which is unaffected by these processes.

A. Rayleigh scattering

In a quasidelectrostatic trap, photon scattering is dominated by Rayleigh scattering [79], with a cross section of $\sigma_R = 8\pi^3\alpha_s^2/(3\epsilon_0^2\lambda^4)$ [89]. Even at the high intensity of $I = 300 \text{ GW/cm}^2$, the Rayleigh scattering rate $W_R = I\sigma_R/\hbar\omega$ is only $\sim 10^3 \text{ s}^{-1}$ for the molecules in Table I.

The maximum amount by which the Rayleigh scattering can be enhanced by the cavity is given by the Purcell factor $F_P = 6\lambda^2\mathcal{F}/(\pi^3w_0^2)$ [90], which is 119 for our cavity. Taking this into account, the heating rate from photon scattering is $< 0.1 \text{ K/s}$ for all molecules in Table I [82], which is negligible in our experiment. Similarly, the low scattering rate means the maximum density limit from reabsorption of scattered light is $> 10^{35} \text{ cm}^{-3}$, which can be ignored [91]. In reality, $F_P = 119$ overestimates the cavity enhancement of the Rayleigh scattering, as effects such as the recoil shift and collisional broadening will shift the scattered photons off resonance with the cavity.

B. Raman scattering

A small fraction of photon scattering events are inelastic. These spontaneous Raman scattering events lead to rotational or vibrational excitation of trapped molecules. Rotational Raman scattering (RRS) occurs in molecules with a nonzero polarizability anisotropy $\Delta\alpha_s$. The molecule absorbs a cavity photon and emits a photon of a different energy, the energy difference accounting for a change in rotational state of the molecule. In linear molecules with zero electronic angular momentum about the symmetry axis, the Raman selection rule is $\Delta J = 0, \pm 2$, where J is the rotational angular momentum of the molecule [92]. RRS from the $J = 0$ ground state of molecules occurs at a rate [57,93]

$$W_{RR} = \sigma_{RR} \frac{I}{\hbar\omega} = \frac{512\pi^5}{135} (1 + 2\rho) \frac{1}{(\lambda')^4} \left(\frac{\Delta\alpha_s}{4\pi\epsilon_0} \right)^2 \frac{I}{\hbar\omega}, \quad (4)$$

where $\lambda' \approx \lambda$ is the wavelength of the scattered photon, $\omega = 2\pi c/\lambda$ is the incident angular frequency, and $\rho = 3/4$ is the depolarization ratio of the Raman transition [94] ($\hbar = h/2\pi$: reduced Planck constant). In rare cases, e.g., for NO, the molecular ground state has nonzero electronic angular momentum about the symmetry axis, in which case Eq. (4) is modified by different selection rules and Placzek-Teller coefficients [95].

Molecules with $W_{RR} \lesssim 70 \text{ s}^{-1}$, such as N_2 , CO , O_2 and HCl , are ideal first candidates for our proposed experiment, as they can be isolated from the buffer gas, and potentially evaporatively cooled, faster than they are rotationally heated (see Sec. V B 5). The RRS cross section scales with $\Delta\alpha_s^2$ and λ^{-4} , so molecules with higher polarizability anisotropies can still be trapped and isolated as described in this work using a trap with $\lambda > 1064 \text{ nm}$ (see Table I).

Vibrational Raman scattering rates in molecules are typically less than $\sim 1 \text{ s}^{-1}$ at 300 GW/cm^2 of 1064-nm light, and can be ignored [96–98].

C. Ionization

The molecules suitable for trapping in Table I have ionization energies $I_0 > 12 \text{ eV}$ and no transitions at any low

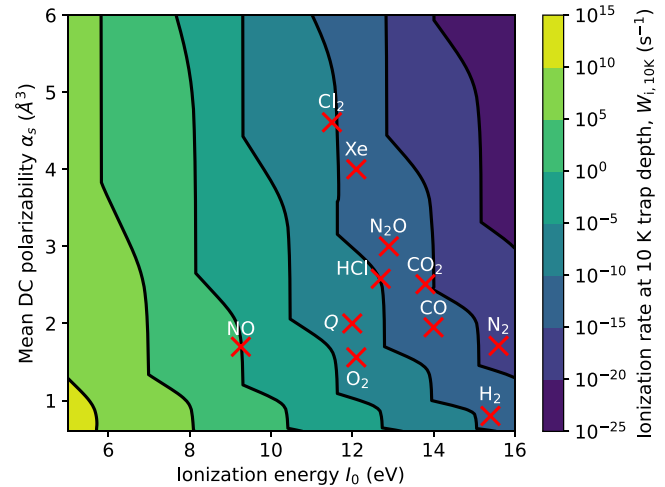


FIG. 2. Ionization rate at 10 K trap depth, $W_{i,10K}$, against ionization energy I_0 and mean DC polarizability α_s . The molecules of Table I (except CS_2 , which is outside the shown region) are marked with red crosses on the plot. Evidently, $W_{i,10K}$ is much more sensitive to the ionization energy than the polarizability.

harmonics of the 1064-nm trap light. Under these conditions, we can approximately estimate the ionization rate W_i of isolated molecules in the trap. A Q molecule with $I_0 = 12 \text{ eV}$ trapped with $I = 300 \text{ GW/cm}^2$ has a Keldysh parameter of 14, meaning nonresonance-enhanced ionization occurs via multiphoton ionization (MPI) [99]. The ionization rate W_i scales as $W_i = \sigma_n I^n$, where $n = 11$ is the number of photons needed to reach the continuum and σ_n is the MPI cross section.

It is difficult to estimate σ_n *ab initio*. As a starting point, we use Popruzhenko's formula [100] for hydrogenlike atoms, which is a Perelomov-Popov-Terent'ev (PPT) ionization formula [101]. The formula matches (within two orders of magnitude) experimental results for ionization rates of noble gases [102,103] and air [104]. PPT formulas also match *ab initio* estimates of ionization rates for polyatomic molecules [105]. Popruzhenko's formula predicts $W_i = 2.8 \times 10^{-9} \text{ s}^{-1}$ for Q . W_i scales down superexponentially with increasing I_0 , meaning molecules with slightly higher ionization energies have substantially smaller ionization rates, as seen in Table I.

The ionization rate can be minimized by either using a molecule with a high ionization energy, or a molecule with a high polarizability which requires less laser intensity for trapping. To compare these approaches, we compute the ionization rate at an intensity for which the trap depth is 10 K , $W_{i,10K} = W_i(I|_{T_{\text{trap}}=10\text{K}})$. This is plotted for different values of the mean DC polarizability α_s and ionization energy I_0 in Fig. 2, ignoring the correction to the trap depth ΔT_{trap} discussed in Appendix A. The near-vertical contours roughly represent lines where the ionization energy corresponds to an integer multiple of the photon energy, so the absorption of an extra photon becomes necessary to ionize the molecule, thereby greatly decreasing the ionization rate. By comparison, the higher intensity necessary for lower polarizabilities has a much smaller influence on the ionization rate. Thus ionization energy is a far more important quantity than polarizability in the selection of suitable molecules, granted that a sufficiently high laser intensity can be achieved.

An alternate way to reduce ionization rates is to trap molecules at a longer wavelength. The ionization rate depends primarily on the number of photons needed to reach the ionization continuum, so molecules with low ionization energies may be suitable for trapping with light at $\lambda > 1064$ nm.

Popruzhenko's formula provides a first estimate of the ionization rate, but can be inaccurate in general. There are many examples where multiphoton ionization occurs through an intermediate multiphoton resonance, which can enhance the ionization rate by several orders of magnitude when compared to Popruzhenko's formula [106–108]. Resonance-enhanced multiphoton ionization (REMPI) is now a routine experimental technique for ionization of different molecules, as will be discussed in Sec. VI. It is challenging to estimate REMPI cross sections a priori, particularly due to the lack of detailed spectra of general molecules that are free of spectral broadening. For this reason, we seek molecules with an *ab initio* ionization rate estimate of $\lesssim 10^{-9}$ s $^{-1}$ ($I_0 \gtrsim 12$ eV) in Popruzhenko's formula as first candidates for our trap, so that even if we ignore the contribution of electronic resonances to the ionization rate, we are still unlikely to see ionization in the trap. We note that limits on the ionization rate can be placed with a room-temperature experiment using our trap light, which is especially helpful for determining the suitability of molecules with higher *ab initio* ionization rates such as NO or CS $_2$ (see Table I).

In a high-density gas, laser-induced breakdown becomes the dominant mechanism for ionization in the beam. We have studied breakdown in high-intensity, CW laser beams in detail, and the results are shown in Appendix G. We have determined that the buffer gas is too low-density for breakdown to be a concern during trap loading.

D. Dissociation

Photodissociation of molecules can occur by two distinctively different mechanisms depending on the character of the light that drives it. The first mechanism is direct electronic excitation to a dissociative state. In principle, any molecular state located above any bond's dissociation threshold is dissociative. In practice, though, excited states above the dissociation continuum can be long-lived, as the probability of direct tunneling out of a quasibound excited state into the dissociation continuum is extremely small due to the Franck-Condon principle [92]. Only certain electronic excitations lead to dissociation. In SCS molecules, the dissociative states are either highly excited quasibound states, which have been probed through absorption of single vacuum-ultraviolet photons [109,110], or excited states above the ionization continuum, as has been seen in multiphoton dissociation experiments using NIR and visible pulsed lasers [108,111–113]. In particular, Ref. [108] finds that dissociation using NIR lasers scales highly nonlinearly with the peak intensity, as expected for multiphoton absorption. Thus, following the arguments on ionization in Sec. IV C showing that simultaneous absorption of enough photons to reach these highly excited states is unlikely and provided Q 's electronic transitions are far from resonant with the low harmonics of the 1064-nm light, we expect not to be limited by this form of dissociation.

The second mechanism, infrared multiphoton dissociation (IRMPD), is usually observed in polyatomic molecules or ions using mid- to long-wavelength infrared light, such as from a CO $_2$ laser at 10 μ m [114], resonant with pure rovibrational transitions. IRMPD is a heating mechanism, so the dissociation probability depends on the total energy absorbed rather than peak intensity, provided the light is near a resonance and above a relatively low threshold intensity [115]. As the latter is easily exceeded with our trap light, we must ensure that the IRMPD will not occur at 1064 nm for our molecules of choice.

The three-step mechanism of IRMPD is explained in detail in [116–118]. Firstly, light tuned to a pure rovibrational transition of a molecule repeatedly excites a vibrational mode, until the anharmonicity of the internuclear potential shifts the transition frequency off resonance with the light. This step is impossible in homonuclear diatomic molecules, which do not admit dipole-allowed, pure rovibrational transitions. Secondly, once excited to a high vibrational energy, in a polyatomic molecule, the different molecular vibrational modes are split into a number of closely spaced energy levels, and a “quasicontinuum” of energy levels forms. In the quasicontinuum, heating and ergodic mixing of vibrational quanta occur. The quasicontinuum cannot form in any diatomic molecules, and is unlikely to form in triatomic molecules, because there are not enough different vibrational modes to form a closely spaced structure [117,119]. Finally, once the molecule's total vibrational energy is higher than the dissociation energy, the molecule soon dissociates through accumulation of excitations in a particular dissociative bond. The molecules in Table I all have ≤ 3 atoms, and therefore are not susceptible to IRMPD.

For molecules with many atoms, IRMPD may still be suppressed because 1064-nm light is several times more energetic than a single vibrational quantum in any molecule. In the dipole and harmonic approximations, rovibrational selection rules only allow molecules to absorb one vibrational quantum of energy at a time [120], so absorption in high harmonics of rovibrational transitions is unlikely, and the IRMPD mechanism cannot begin. In polyatomic molecules that do not contain H atoms, absorption at optical frequencies appears to be much smaller than Rayleigh scattering [88], so it is likely that the trap light is far enough off-resonant from the fundamental vibrational modes to suppress IRMPD. For molecules containing H atoms, NIR frequencies correspond roughly to the third harmonic of a fundamental vibrational mode, and absorption has been seen in room-temperature experiments [121,122]. However, we are not aware of any corresponding data at cold temperatures. Thus, for molecules with more than three atoms the overall likelihood of IRMPD in our trap is unclear, and we therefore do not include them as candidate molecules in Table I.

V. BUFFER GAS DYNAMICS

A. Buffer-gas cooling

The first step toward loading the optical trap is cooling the molecules to cryogenic temperatures through buffer-gas cooling [23]. Molecules of all masses and initial temperatures appear to be amenable to buffer-gas cooling [23,123]. As seen

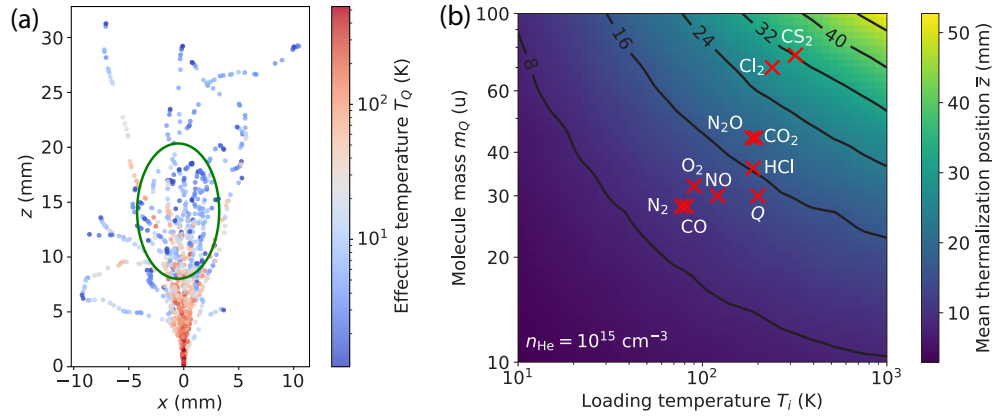


FIG. 3. (a) 2D (xz) projection of trajectories of 50 Q molecules through a cold buffer gas. Each point shows a location of a collision, with the color axis representing the effective temperature $T_Q = m_Q v_Q^2 / 3k_B$ of the molecule at that point. Trajectories continue until the effective temperature reaches the 1.5-K buffer gas temperature. The green ellipse has semi-minor and -major axes equal to the x and z standard deviations respectively, showing the $1\text{-}\sigma$ spread of the positions of molecules when thermalization occurs. (b) Mean z distance traveled, \bar{z} , by 1000 simulated Q molecules into the cold buffer gas as a function of their initial temperature T_i and mass m_Q . Not shown are the x and z standard deviations, which are both less than 10 mm at all T_i, m_Q points. The coordinates corresponding to all molecules of Table I (except H_2 , which is outside the shown region) are marked with a red x .

in Table I, we focus on molecules with a boiling point T_B around 300 K or lower, so they can be loaded into the cold buffer gas in gas phase through a heated fill line without significant thermal load on the cryogenic system. In the design shown in Fig. 1, buffer-gas cooling occurs in two opposing 1.5-K cells to thermalize the molecules to $T = 1.5$ K before buffer-gas loading the trap. This section focuses only on the cooling in the cells, and the loading dynamics are left to Sec. V B.

A cold gas of helium at temperature $T = 1.5$ K is pumped into cells, also at T , at a moderate to low density which we set to be $n_{\text{He}} = 10^{15} \text{ cm}^{-3}$. Q is pumped into the cells through heated fill lines to make up a small fraction of the number density, which we set to be $1/100$. Through collisions with He atoms, Q comes from a warm temperature T_i to T , however it does not solidify as long as it does not collide with the cell walls. To produce a cold gas of Q , we therefore need the mean free path l of Q in the buffer gas to be short compared to the cell dimensions. l is given by [124]

$$l = \frac{v_Q}{\nu} = \frac{1}{n_{\text{He}} \sigma} \frac{v_Q}{v_{\text{rel}}} \stackrel{\text{eq}}{=} \frac{1}{n_{\text{He}} \sigma \sqrt{1 + m_Q/m_{\text{He}}}}, \quad (5)$$

where ν is the Q -He collision frequency, n_{He} is the buffer gas number density, σ the Q -He collision cross section, and v_Q and v_{rel} the Q and mean Q -He relative velocities, respectively. The last equality, labeled with “eq”, holds in thermal equilibrium.

Based on [125–127], we estimate that SCS molecules have collision cross sections with He of order 10^{-14} cm^2 at $T = 1.5$ K, and we take the Q -He collision cross section to therefore be 10^{-14} cm^2 . With $n_{\text{He}} = 10^{15} \text{ cm}^{-3}$, l is 0.34 mm at 1.5 K.

We simulate the thermalization dynamics, using the methods described in Appendix of [76]. Q molecules are drawn by rejection sampling from an effusive initial speed distribution at T_i , directed out of a heated fill line at the origin in the

\hat{z} direction. Each molecule undergoes billiard-ball collisions with He atoms in the buffer gas until it cools to the buffer gas temperature T .

A 2-D projection of 50 molecular trajectories from a fully 3-D simulation is shown in Fig. 3(a). Each point marks a collision, and the color axis represents the effective temperature $T_Q = m_Q v_Q^2 / 3k_B T$ of Q after the collision. The green ellipse shows the $1\text{-}\sigma$ spread of positions where the molecules come to the buffer gas temperature of 1.5 K. The z coordinates of the centers of the green ellipses \bar{z} for different values of m_Q and T_i are shown in Fig. 3(b). Based on this figure, many SCS molecules will thermalize in a 30-mm-tall cell.

B. Buffer-gas loading

With the molecules thermalized to 1.5 K, we next discuss loading them into the optical trap. Since the dipole force is conservative, some supplementary dissipation in the trap volume is required for trapping [1]. Since here Q -He collisions are the only universal source of dissipation, buffer-gas cooling must occur inside the trap volume to achieve loading.

1. Loss-free, equilibrium trapped molecule number

The energy-level splittings associated with the trap frequencies are three orders of magnitude smaller than the buffer gas temperature, so the loading dynamics are semiclassical. Molecules arrive at the loading region after passing through one of the buffer-gas cells, so are already thermalized to 1.5 K. In our closely spaced, opposing cell geometry (Fig. 1), the molecule and He number densities in the loading region are approximately the same as in the cells during loading, with $n_{Q,\text{LR}} = 10^{13} \text{ cm}^{-3}$, and $n_{\text{He}} = 10^{15} \text{ cm}^{-3}$, respectively. If trap losses are negligible, the number density of trapped molecules $n(\mathbf{x})$ during trap loading must eventually follow a Boltzmann distribution [128]:

$$n(\mathbf{x}) = n_{Q,\text{LR}} e^{\eta(\mathbf{x})} P(\mathbf{x}), \quad (6)$$

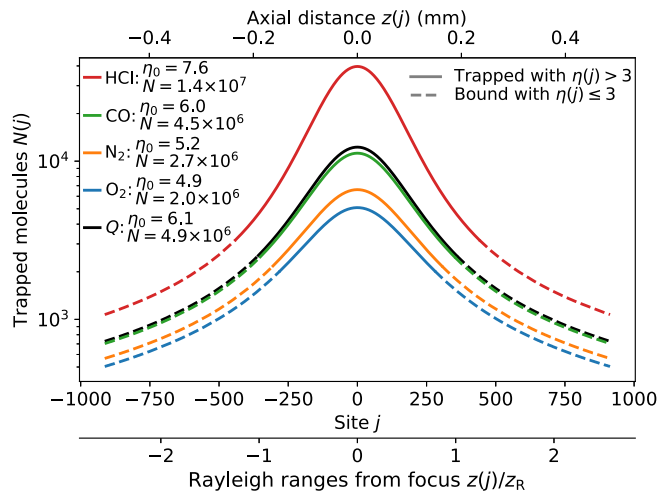


FIG. 4. Number $N(j)$ of trapped molecules per lattice site j during buffer-gas loading for different molecular species, based on Eq. (6), assuming no losses. Solid curves indicate molecules trapped in sites with site depth parameter $\eta(j) = \eta_0 w_0^2/w^2(z(j)) > 3$, dashed curves indicate molecules bound in the trap in weak lattice sites with $\eta(j) \leq 3$. The legend gives the total number of trapped molecules N , given by $N = \sum_j N(j)$, with the sum over all j such that $\eta(j) > 3$.

where $\eta(\mathbf{x}) = |U(r, z)|/k_B T$, and $P(\mathbf{x}) = [\text{erf}(\sqrt{\eta(\mathbf{x})}) - (2/\sqrt{\pi})\sqrt{\eta(\mathbf{x})}e^{-\eta(\mathbf{x})}]$ accounts for the truncation of the distribution at the trap depth.

We now integrate Eq. (6) over space to determine the trapped molecule number. We will index distinct lattice sites with j , refer to their positions as $z(j) = j\lambda/2$, and describe the trap depth of each lattice site by the site depth parameter $\eta(j) = \eta_0 w_0^2/w^2(z(j))$ ($\eta(0) = \eta_0 = T_{\text{trap}}/T$). By integrating Eq. (6) one site at a time, we can determine the total number of trapped molecules $N_Q(j)$ in each lattice site, as well as the total number of trapped molecules $N_Q = \sum_j N_Q(j)$. The sum to $j = \pm\infty$ diverges logarithmically, so we truncate the sum beyond sites where $\eta(j) = \eta_0 w_0^2/w^2(z(j)) \leq 3$. The results are shown in Fig. 4, with $N(j)$ plotted on the y axis and the sum N shown in the legend. The Boltzmann distribution predicts that several millions of molecules will be trapped for each species shown, at peak trapped densities of order 10^{15} – 10^{16} cm^{-3} .

Equation (6) does not, however, indicate the timescale of equilibration. This makes it hard to determine the effect of losses on the number of trapped molecules per site, and it fails to estimate the number of trapped molecules remaining in the trap after the buffer gas and untrapped molecules are pumped out ($n_{Q,\text{LR}} \rightarrow 0$). We therefore consider a microscopic approach to trap loading.

2. Microscopic, ergodic loading model

In our trap, the trap dimensions (set by $w_0 = 8 \mu\text{m}$ and $\lambda = 1064 \text{ nm}$) are much smaller than the mean free path $l = 340 \mu\text{m}$, so our loading model will differ from models used in buffer-gas-loaded magnetic trapping experiments, where l is small compared to the trap dimensions [23].

Starting with an empty trap, any free molecule passing through the trap potential can only be loaded if a collision with

a He atom reduces its energy to below the local trap depth. Of the free molecules that collide with a He atom in the trap, a substantial fraction f_0 will not lose enough energy in the collision to become bound. Since $l \gg w_0$, no other collision will occur in the trap volume for these molecules, so they are lost. The remaining molecules do lose enough energy to initially be bound in the trap, however not all of these molecules will go on to thermalize at the bottom of the trap potential. A fraction f_1 of molecules will be initially bound, but never fall to a total energy consistent with a truncated Boltzmann distribution that would indicate thermalization. Meanwhile, a fraction f_2 (with $f_0 + f_1 + f_2 = 1$) will be initially bound and also go on to thermalize. Molecules which thermalize will live in the trap until they eventually are ejected after a mean number of collisions $k_{Q\text{-He}}$ with the buffer gas.

The Q -He collision time from Eq. (5) is $10 \mu\text{s}$, but in the harmonic approximation the radial and axial orbital periods for a trapped molecule are 600 ns and 18 ns , respectively. Since the true trap potential Eq. (2) is highly nonlinear outside the harmonic approximation, the ergodic approximation can be taken for the motion of Q in the trap. Hence, approximating collisions as equally likely to occur at each time interval, Q 's trajectory need not be integrated to determine its initial conditions for each collision, which are instead drawn randomly from the energy hypersurface. It then becomes computationally simple to track the energy of Q after a number of hard-ball collisions with He atoms drawn from a Maxwell distribution at $T = 1.5 \text{ K}$. The details of these simulations are discussed in Appendix C.

The results of the ergodic loading simulations are shown in Fig. 5 as a function of the site depth parameter η in one particular lattice site. The simulation results do not noticeably depend on the chosen site j except through the site depth parameter $\eta(j)$, so to show their generality, we omit the index j and write the site's depth as η . The loading fractions f_i vary slowly with η . The number of Q -He collisions needed for a thermalized molecule to be ejected from the trap, $k_{Q\text{-He}}$ (right axis), however, grows exponentially with η .

3. Time-dependent, loss-inclusive loading model

Applying these results across all lattice sites, we can estimate the number of trapped molecules $N_Q(j)$ in a lattice site j as well as its time dependence. The approximate model we develop will be limited mostly by three approximations.

(1) The loading fractions $f_i(j)$ and collision rates are computed assuming the trap is empty, which ignores the fact that the number density and energy distribution of molecules in the trap volume is affected by molecules in the trap and molecules recently ejected from the trap. Our approximate model will therefore only strictly be valid in the limit of high trap losses, and this effect leads to an underestimation of $N_Q(j)$ in thermal equilibrium with the buffer gas in the low-loss limit by a factor of about 3.

(2) The simulations are carried out in a truncated harmonic trap with total volume $V_e(j) = w^2(z(j))\lambda/3$ as opposed to the true nonlinear trap potential (see Appendix C). This leads to an underestimation of $N_Q(j)$ by a factor of 1.5–2.

(3) The model will compute $N_Q(j)$ without explicitly determining the local density distribution in the trap, and will

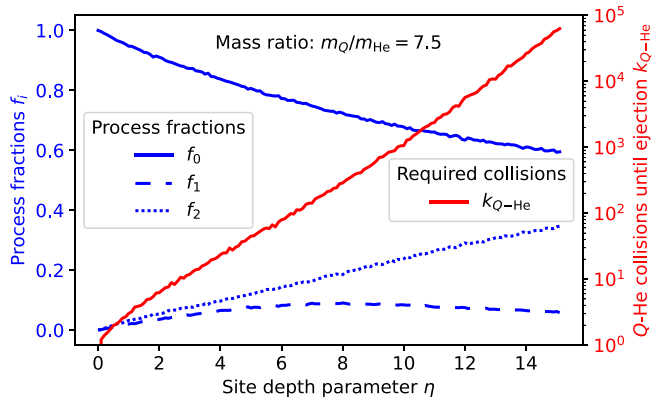


FIG. 5. Ergodic loading simulations in a single lattice site. As a function of the site depth parameter η , we show the loading fractions of an unbound molecule undergoing a collision in the trap volume on the left axis. The fractions are the following: f_0 (solid blue curve): molecule undergoes a collision in the trap but does not lose enough energy and immediately escapes the trap; f_1 (dashed blue curve): molecule does lose enough energy to not immediately escape the trap, but in subsequent collisions never loses enough energy to fall to a thermal Boltzmann distribution; f_2 (dotted blue curve): molecule does lose enough energy to not immediately escape the trap, and in subsequent collisions loses enough energy to eventually fall below a Boltzmann distributed energy. For a molecule that thermalizes, the number of Q -He collisions needed for it to be ejected from the trap, k_{Q-He} (red curve), is shown on the right axis.

therefore not completely account for out-of-equilibrium loss rates.

With these approximations in mind, we can write down an equation for $dN_Q(j)/dt$. Molecules will be loaded into an empty trap at a rate $n_{Q,LR}(t)V_e(j)v(n_{He}(t))f_2(j)$, dependent on the number of free molecules in the trap volume $n_{Q,LR}(t)V_e(j)$, the Q -He collision frequency $v(n_{He}(t))$, and the fraction of collisions in $V_e(j)$ that lead to loading $f_2(j)$. Molecules will be collisionally ejected from the trap at a rate $[v(n_{He}(t))/k_{Q-He}(j)]N_Q(j)$, and two-body collisions between trapped molecules lead to an additional loss term $[\beta_{Q-Q}/V_e(j)]N_Q^2(j)$, where β_{Q-Q} is the Q - Q two-body loss coefficient. Rotational Raman scattering (RRS) leads to an additional loss term Γ_{RR} dependent on the RRS rate W_{RR} . We neglect a noncollisional one-body loss term $-\Lambda N_Q(j)$, because ionization, dissociation, and recoil heating are small (see Sec. IV). Other sources of trap heating are also small, as discussed in Sec. D. Overall,

$$\frac{dN_Q(j)}{dt} = n_{Q,LR}(t)V_e(j)v(n_{He}(t))f_2(j) - \frac{v(n_{He}(t))}{k_{Q-He}(j)}N_Q(j) - \frac{\beta_{Q-Q}}{V_e(j)}N_Q^2(j) - \Gamma_{RR}. \quad (7)$$

Note that in the two-body loss term, the effective volume is the full simulation volume $V_e(j)$, as opposed to a commonly used $V_{eff} = \sqrt{\pi/2}w_0^2\lambda/\eta^{3/2}$ [129]. This effective volume V_{eff} is only appropriate when the density distribution in the trap is close to a Boltzmann distribution. Our approximate loading model, on the other hand, is only strictly valid when losses are high ($\beta_{Q-Q} \gtrsim 10^{-11}$ cm³/s), in which case the trap

density distribution is pinned near a constant value $n_Q(j) \approx \sqrt{v(n_{He}(t))f_2(j)n_{Q,LR}(t)/\beta_{Q-Q}}$. The molecules are therefore evenly distributed over the volume $V_e(j)$ in the high-loss limit. In the low-loss limit, on the other hand, the choice of the effective two-body loss volume is not critical.

Equation (7) can be integrated once β_{Q-Q} and Γ_{RR} are specified. In magnetic traps, two-body loss is usually caused by spin-changing inelastic collisions between trapped particles, and typical values of β_{Q-Q} range from 4×10^{-11} cm³/s [28] to 9×10^{-13} cm³/s and lower [130]. Our trap, however, is insensitive to the molecules' internal state, so we are likely not limited by this kind of loss. In Appendix E 2, we show that collision-induced absorption, seen in O₂ gases, also does not cause significant two-body loss when trapping O₂ at the densities expected in our experiment. In optical trapping experiments on molecules, particularly alkali molecules, a high two-body loss rate is observed. In this so-called “universal loss,” a close to unity fraction of collisions between molecules in the trap are lossy. The mechanism is discussed in Sec. E 1, but in short, we believe universal loss is unlikely in our experiment due to the weak interactions between, and the high excitation energies of, SCS molecules, and consider universal loss only as a possible “worst case scenario”. It is more likely that β is small enough to be ignored, and the loss is dominated by the other loss terms in Eq. (7).

The loss due to RRS, Γ_{RR} , has a complicated form, which is detailed in Appendix F. Nevertheless, the effect of Γ_{RR} is simple. During buffer-gas loading, rotational cooling is efficient [123], and RRS does not lead to substantial loss. Once the buffer gas is removed, rotational heating causes exponential decay of the ground state trapped population at a rate W_{RR} .

4. Loading simulation results

Integrating Eq. (7) to find approximate values for $N_Q(t)$ is done in four stages, and the results are shown in Fig. 6. We start in Fig. 6(a) with the simplest case of negligible two-body loss, and show the evolution of trapped Q as a function of time for various optical intensities. We begin the simulation by turning on the trap at $t = -50$ ms with $n_{He} = 10^{15}$ cm⁻³ and $n_{Q,LR} = 10^{13}$ cm⁻³. The figure shows the trapped molecule numbers coming to equilibrium within a few ms.

The pumpout begins at $t = 0$ ms, when the cryogenic shutter actuates in 1 ms to stop flow into the loading region. We conservatively assume molecules will cryopump to the surface of the shutter, rather than bounce off it, to underestimate the trap loading during the pumpout, and conservatively assume the He buffer gas will take longer to evacuate the loading region to overestimate the trap losses during pumpout. To this end, we set the He and molecule pumpout timescales from the loading region to be 2 ms and 0.5 ms, respectively. After $t = 0$ ms, n_{He} and $n_{Q,LR}$ decay exponentially with these pumpout timescales. To model the effect of He film formation on the outside of the buffer-gas cells, we let n_{He} saturate at 10^{11} cm⁻³ for the remainder of the simulation [131,132]. The trapped densities all rapidly re-equilibrate to the new loading region densities, until after about 10 ms, when the loading region densities are so small that the trap is isolated and the trapped molecule number is constant.

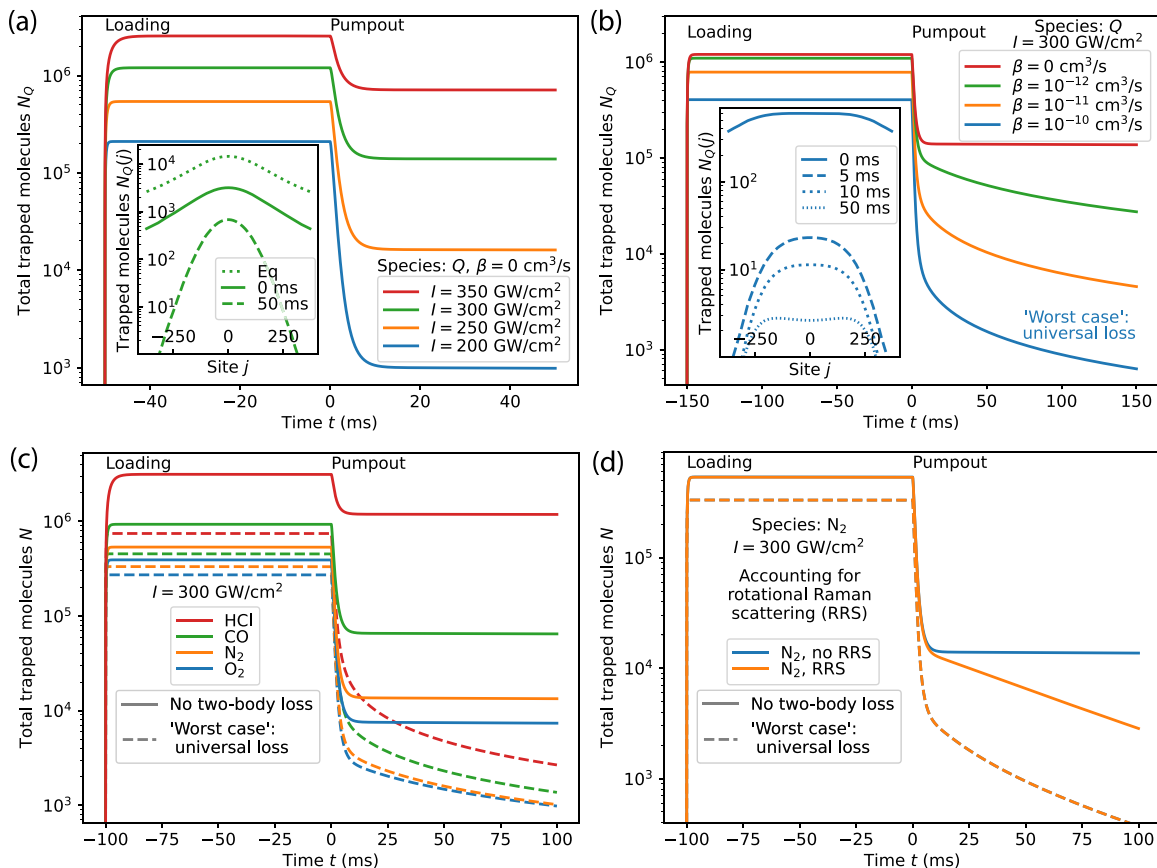


FIG. 6. Number of trapped molecules $N_Q(t)$ from Eq. (7) for different scenarios. Loading occurs at negative t , with He density $n_{\text{He}} = 10^{15} \text{ cm}^{-3}$ and Q density $n_{Q,\text{LR}} = 10^{13} \text{ cm}^{-3}$. Pumpout to produce an isolated sample begins at $t = 0$, after which n_{He} and $n_{Q,\text{LR}}$ exponentially decay with a timescale of 2 and 0.5 ms, respectively. n_{He} saturates at 10^{11} cm^{-3} to model He film desorption dynamics. In (a), Q is treated assuming no two-body loss for various optical intensities I . Inset shows the distribution of molecules across lattice sites at $t = 0$ ms (solid curve) and $t = 50$ ms (dashed curve). The $t = 0$ ms curve can be compared to the analytic result from Eq. (6) (dotted curve), which shows that the approximate model Eq. (7) underestimates $N_Q(j)$ during loading in the low-loss limit by a factor of 6. In (b), Q is treated with fixed intensity $I = 300 \text{ GW/cm}^2$, but varying two-body loss coefficients β_{Q-Q} . The highest value of $\beta_{Q-Q} = 10^{10} \text{ cm}^3/\text{s}$ corresponds to the “worst case” of universal loss, which we believe to be unlikely in our trap (Appendix E 1). Inset shows the distribution of molecules across lattice sites at different times for the case of universal loss. In (c), we integrate Eq. (7) for N_2 , CO , O_2 , and HCl with $I = 300 \text{ GW/cm}^2$, ignoring rotational Raman scattering (RRS). For each molecule, we consider the case of no two-body loss (solid curves), as well as the unlikely “worst case” of universal loss (dashed curves). β_{Q-Q} coefficients for universal loss are computed as in Appendix E 1. For the case of no two-body loss, the peak trapped densities at $t = 100$ ms (averaged over the central lattice site volume $V_\epsilon(0)$) are $1.7 \times 10^{12} \text{ cm}^{-3}$ (O_2), $3.1 \times 10^{12} \text{ cm}^{-3}$ (N_2), $1.4 \times 10^{13} \text{ cm}^{-3}$ (CO), and $2.3 \times 10^{14} \text{ cm}^{-3}$ (HCl). In (d), we integrate Eq. (7) for N_2 , comparing the cases of including and excluding RRS to exemplify its effect. The effect of RRS is modeled in Appendix F.

With increasing intensity, the number of molecules trapped during the loading phase increases, and also the fraction of these molecules retained in the trap after pumpout increases. Our proposed experiment, with $I = 300 \text{ GW/cm}^2$, appears to trap about 10^5 Q molecules in our approximate model. The inset in Fig. 6(a) shows the evolution of the number of molecules over time in each site for $I = 300 \text{ GW/cm}^2$. Just before pumpout, at $t = 0$ ms, the trapped molecule numbers predicted by Eq. (7) (solid curve) resemble a Boltzmann distribution (dotted curve), except that the approximations involved in Eq. (7) lead to an underestimation of the trapped molecule number by a factor of 6. After 50 ms, when the trap is isolated from background-gas collisions, we see that molecules near the focus of the trap are retained more than

molecules far from the focus, since the trap depth $\eta(j)$ is higher.

In Fig. 6(b), we consider the effect of two-body losses. The details of the pumpout are the same as in Fig. 6(a), but the integration time is increased so that the long-time behavior is visible. The blue curve, with $\beta_{Q-Q} = 10^{-10} \text{ cm}^3/\text{s}$, represents universal loss, while the red curve, with $\beta_{Q-Q} = 0 \text{ cm}^3/\text{s}$, represents no two-body loss. We see that two-body loss leads to a reduction in the trapped molecule number during loading, the fraction of molecules that survive the pumpout, and the number of molecules in the long-time limit. Roughly speaking, in the high- β_{Q-Q} limit, each order-of-magnitude reduction in β_{Q-Q} leads to an order-of-magnitude increase in the trapped molecules 200 ms after pumpout.

The inset of Fig. 6(b) shows how molecules are distributed among lattice sites in the universal loss limit ($\beta_{Q-Q} = 10^{-10} \text{ cm}^3/\text{s}$). Pinning of the trapped molecule number near the trap focus is clearly visible, which retroactively justifies the use of V_e as the effective two-body loss volume instead of V_{eff} . With universal loss, only a few molecules per lattice site survive after the buffer gas is pumped out, but because the molecules are spread over many lattice sites, the total number of trapped molecules remains large enough for sensitive detection schemes to detect them (see Sec. VI).

Third, we consider some real molecules (N_2 , CO , O_2 , HCl) in Fig. 6(c). We ignore RRS in this figure for clarity, and treat it separately. For each molecule, we recompute the parameters $f_2(\eta(j))$ and $k_{Q-\text{He}}(\eta(j))$, which change with the molecular mass and η_0 , and then separately integrate the case of no two-body loss (solid curves) and universal loss (dashed curves) to demonstrate a best and worst case scenario for the number of each molecule we can expect to trap. Even our worst case estimates based on universal loss suggest thousands of molecules will be trapped at peak densities of 10^{11} cm^{-3} (at 100 ms, averaged over the center lattice site volume $V_e(0)$), which will be enough to demonstrate trapping. In the case of no universal loss, on the other hand, about 10^4 O_2 and N_2 molecules, 10^5 CO molecules, and 10^6 HCl molecules can be trapped. These correspond to peak trapped densities (at 100 ms, averaged over the central lattice site volume $V_e(0)$) of $1.7 \times 10^{12} \text{ cm}^{-3}$ (O_2), $3.1 \times 10^{12} \text{ cm}^{-3}$ (N_2), $1.4 \times 10^{13} \text{ cm}^{-3}$ (CO), and $2.3 \times 10^{14} \text{ cm}^{-3}$ (HCl).

Finally, we exemplify the effect of RRS in Fig. 6(d) by studying its impact on N_2 (see Appendix F). During buffer-gas loading, the curves for the case without RRS (blue) and with RRS (orange) are indistinguishable, owing to efficient rotational cooling by the buffer gas. After the buffer-gas pumpout, exponential decay of the rotational-ground-state, trapped population is observed at the rate W_{RR} .

5. Evaporative cooling and other considerations

In our models, for the case when β_{Q-Q} and W_{RR} are small, we have so far ignored the evaporative effect of $Q-Q$ elastic collisions after the buffer-gas pumpout. They will lead to additional Q loss, but also decrease the sample temperature and thus increase η_0 through evaporative cooling, making them fundamentally different in nature to the losses included in Eq. (7) [133]. We compute the initial evaporation timescale at constant η_0 [134,135] to be $N_Q(0)/\dot{N}_Q(0) = \tau_{\text{ev}} = 15 \text{ ms}$ for the central lattice site of our trap, 1.5 times less than [134]. Therefore, for species with $W_{\text{RR}} < 70 \text{ s}^{-1}$, at least some amount of evaporation can be achieved initially, allowing for a reduction of the trap depth which in turn proportionally reduces the RRS rates.

For molecules with low losses, we expect similar evaporative cooling dynamics to [134], where 800 optically trapped Rb atoms are evaporated to 40 atoms with $\eta \sim 5$, resulting in a 1000-fold reduction in temperature and increase in phase-space density. At the now reduced optical intensity required to maintain trapping of tens of molecules per lattice site at $\sim 1.5 \text{ mK}$ (phase-space density $\sim 10^{-4}$), the sites could be combined using a bichromatic light field [136]. The resulting

sample of thousands of molecules at mK temperatures could be evaporated further towards the ultracold regime.

We have also thus far ignored the effect of trapped He atoms. Although a small amount of sympathetic evaporative cooling can be expected from the rapid evaporation of trapped He [137], the number of He atoms that will survive the buffer-gas pumpout is negligible due to their low trap depth of $\eta_0 = 0.6$.

One final consideration during He pumpout is the buffer-gas “wind” dragging molecules out of the trap, as observed in buffer-gas-loaded magnetic traps [132]. In our trap, the Q -He collision frequency is slow compared to the trap frequencies, so the Q position and velocity in the trap is randomized between collisions. The wind therefore does not provide a unidirectional drag force on trapped molecules, so need not be considered in our trap.

VI. DETECTION

To detect the molecules in the trap both during and after loading, a sensitive and background-free scheme is required. Absorption or fluorescence detection techniques, commonly used for cold and ultracold atoms, are challenging to implement for most SCS molecules due to the lack of optical cycling transitions.

Resonance-enhanced multiphoton ionization (REMPI) of molecules with an intense UV laser pulse, in combination with the detection of the charged products, is both sensitive and background-free [138]. The UV laser pulses can be derived from a frequency-converted, tunable dye laser, and a microchannel plate (MCP) can serve as a detector. Due to its resonant nature, REMPI only ionizes a given species, but not any other species in the background gas. It can also resolve internal states, allowing a measurement of the rovibrational temperature of the molecules. Furthermore, differential AC Stark shifts from the trap light will likely lead to the resonant frequencies for trapped and untrapped molecules to be different on the order of the trap depth of $\sim 200 \text{ GHz}$ ($\sim 10 \text{ K}$). Thus, given a narrow enough resonance, REMPI can distinguish between trapped and untrapped molecules. For example, [139] has used REMPI to resolve different rotational levels in N_2 at 15 K, corresponding to a resolution of better than 120 GHz. This also opens up the intriguing possibility to selectively remove molecules with a certain kinetic energy from the trap, which could be of use in forced evaporative cooling schemes, or to forcibly remove rotationally excited molecules from the trap.

Although REMPI is only applicable to molecules which have selection-rule-allowed multiphoton transitions [140], the technique is widely applicable. In addition to all of the molecules listed in Table I, REMPI has been demonstrated on other symmetric tops like NH_3 [141] and benzene [142], asymmetric tops like SO_2 [143], H_2O [144], methanol and ethanol [145], radicals like NH [140], SF_2 [146] and OH [147], aromatics and organic compounds [148], and a wide variety of other atomic and molecular species [149].

An alternative scheme is nonresonant ionization of molecules in a tightly focused, ultrashort laser pulse, and subsequent characterization of the products using time-of-flight mass spectrometry (TOFMS) [102,107,108]. This allows for

the simultaneous detection of arbitrary molecular species in the trap and thus the monitoring of chemical populations as a function of time during cold chemical reactions. However, trapped and untrapped molecules cannot be easily distinguished with this technique, leading to a large background signal especially during the loading phase. Moreover, the long TOFMS path and ion optics required to distinguish different mass products will make the technique challenging in our experiment. We note that, in principle, an electron beam could be used for nonresonant ionization, but this will lead to a larger background signal compared to a laser beam as gas outside the focal volume will also be ionized.

Finally, the trap light scattered off the molecules could be used for detection. However, even for the high intensities assumed here, the Rayleigh scattering rate is only $\sim 10^3 \text{ s}^{-1}$ (see Sec. IV A), which will be difficult to distinguish from other sources of scattered light in a realistic apparatus. This could in principle be overcome by using a second resonant, but otherwise empty, cavity to enhance the Rayleigh scattering rate [90].

VII. SUMMARY AND OUTLOOK

In this work, we have studied trapping small, chemically stable (SCS) molecules in a deep, very far-off-resonant, quasielectrostatic dipole trap formed by a tightly focused, high-intensity optical cavity. We have analyzed the trapping and buffer-gas loading dynamics, and the potentially harmful effects of the high-intensity laser light on the molecules. For the examples of N_2 , CO , O_2 , and HCl , we conclude that on the order of a million molecules can be loaded into the trap, and a large fraction can be retained after removing the buffer gas to produce an isolated sample. Evaporative cooling can be used to further reduce the temperature of the trapped sample, possibly deep into the mK regime. Other molecules shown in Table I, such as CO_2 and N_2O , may be similarly trapped, but might require a longer wavelength than the 1064-nm light proposed here to reduce their rotational Raman scattering or ionization rates. Likewise, H or H_2 could be trapped if the intensity can be further increased by a factor of two over the demonstrated value, or if the temperature of the buffer gas can be further reduced, e.g., with additional buffer-gas cells cooled below 1 K with a ^3He pot.

Although this work has focused on a sub-class of linear molecules, we see no obvious reasons why our proposed trap cannot be used on other classes of SCS molecules. For example, SO_2 ($\alpha_s = 3.8 \text{ \AA}^3$, $I_0 = 12.3 \text{ eV}$ [53]) and H_2O ($\alpha_s = 1.5 \text{ \AA}^3$, $I_0 = 12.6 \text{ eV}$ [53]) are small but nonlinear atmospheric gases which may be trapped without significant modification to the trap design presented here. We have also focused on molecules which can be loaded into the buffer-gas cells from a heated fill line. Future renditions of our experiment could instead use laser ablation to seed molecules into the buffer gas, opening up the possibility of trapping heavy molecules and radicals that are of interest in atmospheric and interstellar chemistry [18], and in tests of the Standard model [15,150].

Moreover, the literature on high-intensity, continuous-wave laser–molecule interactions is sparse, so although we have determined that molecules with ≤ 3 atoms and $I_0 \geq$

12 eV are unlikely to be destroyed by the trap light, this does not necessarily imply that other molecules will be destroyed. We believe that many molecules outside these constraints will still be suitable for trapping. In the case of ionization, because of the approximations made in Popruzhenko’s formula used here to estimate the ionization rate W_i , we here have placed a rather conservative constraint of $W_i < 10^{-9} \text{ s}^{-1}$. By measuring the ionization rates of molecules in our high-intensity cavity, without even the need for buffer-gas cooling, the robustness of molecules against ionization can be directly determined. As for dissociation, the arguments made above do not obviously rule out molecules like the planar BF_3 ($\alpha_s = 2.4 \text{ \AA}^3$, $I_0 = 15.7 \text{ eV}$ [53]) or the spherical top SF_6 ($\alpha_s = 4.5 \text{ \AA}^3$, $I_0 = 15.3 \text{ eV}$ [53]) as potential trap candidates. Although they have more than three atoms, initial excitation of vibrational modes may be suppressed because the 1064-nm trap light is so far from the fundamental vibrational modes in these molecules. Similarly, although room-temperature data for hydrogen-containing molecules with more than three atoms, like CH_4 ($\alpha_s = 2.5 \text{ \AA}^3$, $I_0 = 12.6 \text{ eV}$ [53]) and CH_3OH ($\alpha_s = 3.2 \text{ \AA}^3$, $I_0 = 10.8 \text{ eV}$ [53]), indicate some absorption at near-infrared frequencies [121,122], it is unclear that this will lead to infrared multiphoton dissociation (IRMPD) at cold temperatures. Deuteration and halogenation of these molecules may also reduce the risk of IRMPD by lowering their fundamental vibrational frequencies. Measurements of molecular ionization and dissociation rates in our cavity provide valuable information about the kinds of molecules we can trap in our proposed experiment, but also fill a gap in the literature surrounding the interaction of high-intensity, continuous-wave lasers with molecules.

Nevertheless, even the cold chemical reactions of very simple molecules such as those in Table I are difficult to simulate, and therefore interesting to study [17,18]. At cold and ultracold temperatures, accurate descriptions of chemical reactions require a fully quantum mechanical treatment [17,18,151,152]. Despite this, state-of-the-art calculations, including that of the predissociative state lifetime of cold collisional complexes of diatomic alkali molecules [153], still rely on semiclassical approximations, which are not valid for SCS molecules (see Ref. [152] and Appendix E 1). Our proposed trap is insensitive to most molecular properties and could be loaded with multiple different molecular species simultaneously, allowing for the study of a diverse range of cold chemical reactions. Our trap will therefore provide valuable information about the transition between classical and quantum mechanical descriptions of chemical reactions, and help benchmark new theoretical and numerical techniques to compute the dynamics of cold chemical reactions.

Spectroscopy on cold and ultracold, trapped molecules is another promising application of our trap. For example, radio searches for interstellar organic molecules are partly limited by a lack of available experimental data to compare to observed spectra [19,154]. In many cases, computational models are being used to augment experimental observations of molecular spectra, leading to their more frequent use in molecule searches [155]. Laboratory measurements of cold molecular spectra in our trap will therefore not only directly assist interstellar molecule searches, but also provide valuable

data to calibrate computational models and prove their general accuracy. Likewise, astrophysical studies of the variation of the proton-to-electron mass ratio μ from the observation of molecular spectra, such as of CH_3OH , would benefit from improved laboratory measurements of the relevant transitions [14]. Atomic- or molecular-beam-based precision measurements [15,156,157] could be improved upon by trapping the atoms or molecules at 1.5 K instead, thereby increasing the interaction time and averaging some systematic effects related to the particles' motion such as Doppler shifts. The light shift from the trap light can be removed by releasing the cold molecules from the trap during measurements. Alternatively, a magic wavelength for the trap light [158–161] can be chosen such that the differential light shift of a given transition is reduced (see Appendix A).

ACKNOWLEDGMENTS

This work was supported by the Gordon and Betty Moore Foundation (Grant No. 9366), the U.S. Department of Energy, Office of Science, National Quantum Information Science Research Centers, Quantum Systems Accelerator (QSA, No. 1009 DE-AC02-05CH11231), the NASA Jet Propulsion Laboratory (JPL) (Grant No. 1669913), the Chan Zuckerberg Initiative (Award No. 2021-234606), and Thermo Fisher Scientific (Award No. AWD00004352). A.S. acknowledges support from the Eleanor Sophia Wood Travelling Scholarship. L.M. acknowledges support from the Alexander von Humboldt Foundation through a Feodor Lynen Fellowship. We would like to thank Ben Augenbraun, John Doyle and the members of his research group, Arthur Christianen, Bretislav Friedrich, Yair Segev, Tanya Zelevinsky, and Adrienne Zhong for fruitful discussions, and Howard Padmore for conducting mirror surface profile measurements.

APPENDIX A: ROTATIONAL STATE HYBRIDIZATION AND EXTRA TRAP DEPTH

Equation (1) is an approximate expression for the trap depth. Here, two corrections are discussed: firstly, the mean dynamic polarizability $\alpha_s(\lambda)$ at $\lambda = 1064$ nm is usually slightly larger than the mean DC polarizability α_s used in Eq. (1). A correction of order $(\lambda_1/\lambda)^2 \sim 5\%$, where λ_1 is the wavelength of first electronic excitation of the given molecule, may be warranted for many of the molecules in Table I [79].

The correction is difficult to estimate accurately for most molecules, but is in any case of little consequence to the experiment.

The second correction to Eq. (1) is a result of the hybridization of the rotational states of the molecule, and can have large consequences for the trapping of molecules with large polarizability anisotropies $\Delta\alpha_s$. In general, symmetric top molecules have a different polarizability along their symmetry axis (α_{\parallel}) and perpendicular to this axis (α_{\perp} : $\Delta\alpha_s = \alpha_{\parallel} - \alpha_{\perp}$, $\alpha_s = (\alpha_{\parallel} + 2\alpha_{\perp})/3$). In this analysis, these polarizabilities are assumed to be constant within any given rotational band. In a field-free setting, the rotational eigenstates of a molecule will be thermally populated such that there is no molecular alignment. However, optical fields of sufficient intensity will dress these rotational states and align molecules so that their maximally polarizable axis aligns with the optical polarization [49,162]. Linear molecules are described by the Hamiltonian [49,84]

$$H = BJ^2 - \frac{E_0^2}{4}(\alpha_{\parallel} \cos^2 \theta + \alpha_{\perp} \sin^2 \theta). \quad (\text{A1})$$

Here, θ is the angle between the molecule's symmetry axis and the electric field with amplitude E_0 in a molecule-fixed frame, J is the rotational angular momentum of the molecule, and B is the rotational constant. The time-independent Schrödinger equation takes the form of an oblate spheroidal wave equation [49,84]

$$\left[-\frac{d}{dz} \left[(1-z^2) \frac{d}{dz} \right] + \frac{m^2}{1-z^2} - \frac{\Delta\alpha_s E_0^2}{4B} z^2 \right] \psi_{\tilde{J},m} = \left(\frac{u_{\tilde{J},m}}{B} + \frac{\alpha_{\perp} E_0^2}{4B} \right) \psi_{\tilde{J},m}, \quad (\text{A2})$$

where $z = \cos \theta$, m is the projection of the angular momentum onto the optical polarization axis, \tilde{J} is the quantum number which adiabatically turns into J in the limit of zero electric field, and $\psi_{\tilde{J},m} e^{im\phi}$ and $u_{\tilde{J},m}$ are the eigenfunction and energy of the state with quantum numbers \tilde{J}, m , respectively, where ϕ is the azimuthal angle about the optical polarization axis. The solutions for $\psi_{\tilde{J},m}$ in Eq. (A2) are the angular oblate spheroidal functions $S_{|m|\tilde{J}}$ as defined in section 21.6.4 of [163]. The eigenvalues of Eq. (A2), and hence the energies $u_{\tilde{J},m}$, are readily computed using standard libraries (e.g., `scipy.special.obl_cv` of Ref. [164]). For $\Delta\alpha_s E_0^2/4B \ll 1$, we can write a power series expansion for $u_{\tilde{J},m}$ (see Sec. 21.8.1 in [163]), from which the trap potential $U_{\tilde{J},m}$ is given by

$$U_{\tilde{J},m} = u_{\tilde{J},m} - B\tilde{J}(\tilde{J} + 1) \quad (\text{A3})$$

$$= -\frac{\alpha_s E_0^2}{4} - \frac{1}{2} \left[\frac{1}{3} - \frac{(2|m| - 1)(2|m| + 1)}{(2\tilde{J} - 1)(2\tilde{J} + 3)} \right] \frac{\Delta\alpha_s E_0^2}{4} + \left[\frac{-(\tilde{J} - |m| + 1)(\tilde{J} - |m| + 2)(\tilde{J} + |m| + 1)(\tilde{J} + |m| + 2)}{2(2\tilde{J} + 1)(2\tilde{J} + 3)^2(2\tilde{J} + 5)} \right. \\ \left. + \frac{(\tilde{J} - |m| - 1)(\tilde{J} - |m|)(\tilde{J} + |m| - 1)(\tilde{J} + |m|)}{2(2\tilde{J} - 3)(2\tilde{J} - 1)^2(2\tilde{J} + 1)} \right] \frac{1}{B} \left(\frac{\Delta\alpha_s E_0^2}{4} \right)^2 + B \left(O \left(\frac{\Delta\alpha_s E_0^2}{4B} \right)^3 \right). \quad (\text{A4})$$

For the special case of $\tilde{J} = 0$ and $m = 0$, we have

$$U_{0,0} = -\frac{\alpha_s I}{2\epsilon_0 c} - \frac{\Delta\alpha_s^2 I^2}{270B\epsilon_0^2 c^2} + B \left(O \left(\frac{\Delta\alpha_s I}{2B\epsilon_0 c} \right)^3 \right), \quad (\text{A5})$$

where $I = \epsilon_0 c E_0^2 / 2$ is the optical intensity. In the main text, we use $U_{0,0}$ for the trap potential U , and define the trap depth as $T_{\text{trap}} = \max|U_{0,0}|/k_B$, and the extra trap depth resulting from molecular alignment as $\Delta T_{\text{trap}} = T_{\text{trap}} - \alpha_s I / 2\epsilon_0 c k_B$.

For some of the molecules in Table I, including those treated in the detail in the main text, ΔT_{trap} is much smaller than 1 K, and the degree of alignment (computed using the Hellmann-Feynman theorem as described in Ref. [49]) is small. These molecules are trapped in barely hybridized rotational ground states. However, some of the molecules on the list, such as CO_2 , N_2O , Cl_2 , and CS_2 , see a substantial increase in the trap depth due to rotational alignment, which scales nonlinearly with the intensity around 300 GW/cm^2 . For these molecules, the character of the rotational ground state is highly aligned with the optical polarization (note that this effect is here ignored in the calculation of rotational Raman scattering rates).

The buffer gas collision frequencies ($\sim 10^5 \text{ s}^{-1}$) and trap frequencies ($< 100 \text{ MHz}$) are small compared to the rotational constants of the molecules in Table I ($> 3 \text{ GHz}$). Thus trapped molecules adiabatically follow the dressed rotational ground state as they traverse the trap. We note in passing that this is unlike a previously proposed experiment to trap polar molecules in microwave fields [34]. In particular, the polarizability at 1064 nm is independent of the rotational state, so avoided crossings do not open up avenues for rotational state changes during trap traversal in our experiment, as opposed to [34].

In precision spectroscopy of atoms, magic wavelength schemes [158] are used to cancel differential light shifts between two given states by making the dynamic polarizability $\alpha_s(\lambda)$, and thus $U_{J,m}$, of the states equal by choice of a suitable (“magic”) trap light wavelength. To first order in intensity, a magic wavelength can still be found for molecules, although the wavelength must be tuned to not simply cancel the difference in each state’s $\alpha_s(\lambda)$ (except in the special case of $\tilde{J} = 0$ [159,160]), but rather, to cancel the first-order term in Eq. (A3) [161]. In general, more magic parameters are required to cancel higher-order terms in Eq. (A3). Rotational state hybridization can represent a large additional contribution ΔT_{trap} to T_{trap} at $I = 300 \text{ GW/cm}^2$ (up to 37% of T_{trap} in the case of CS_2) when compared to other corrections [162], such as: nonlinear corrections due to electronic and vibrational contributions to molecular hyperpolarizabilities, which typically contribute a few mK in additional trap depth at $I = 300 \text{ GW/cm}^2$ [165–169], and; linear corrections due to higher order multipoles in the multipole expansion [160,161], which typically are orders of magnitude smaller than the leading linear term [170]. Small differences in the polarizability components $\alpha_s(\lambda)$ and $\Delta\alpha_s(\lambda)$ within each rotational band [161] additionally modify the analysis starting with Eq. (A1).

APPENDIX B: HEAT LOAD FROM SCATTERED TRAP LIGHT

A major heat load on the cryogenic system in our experiment is scattering of the high-intensity cavity light. Our mirrors will be superpolished to $\sim 1 \text{ \AA RMS}$ (root-mean-

square) surface roughness, and the resultant scattered light will be a few hundred mW. From white light interferometry measurements of our previous mirrors’ surface profiles, we have determined the angular distribution of scattered light [171–173]. About half of the scattered light is diffusely scattered, and is managed by placing the mirrors more than 10 mm from the apertures in the 50-K shields. The other half is scattered into a small cone around the cavity mode. From ray-tracing this scattered light through the near-concentric cavity, we know this light will be incident on either a buffer-gas cell, or the inside of one of the cryocooler’s radiation shields, rather than the outside of the radiation shields. The buffer-gas cells will be polished and highly reflective, so light incident on them will be reflected towards the radiation shields (mostly the 4-K shield). We aim to absorb the scattered light that misses the buffer-gas cells on the 50-K shields rather than the 4-K shields, due to their larger cooling capacity. This is achieved by designing the 50-K shields with a smaller angular size than the 4-K shield apertures when viewed from the opposite mirror, so the scattered light will be absorbed on the nonreflective (NR) material on the 50-K shields shown in Fig. 1.

An alternative approach to handle the scattered light is to conically indent the radiation shields around the cavity mode, allowing the apertures to be closer to the cavity focus, and therefore smaller, so that almost no scattered light enters the cryogenic system in the first place. This approach has small consequences for the pumpout timescale, and has not been investigated thoroughly.

All other heat loads from scattering of the high-intensity light, including Rayleigh scattering from the buffer gas and trapped molecules (nW) and scattering of transmitted input light not matched into the cavity mode ($< 1 \text{ mW}$), are negligible for our experiment.

APPENDIX C: DETAILS OF ERGODIC LOADING SIMULATIONS

At their core, the ergodic loading simulations work by storing the energy E of Q molecules, and assigning initial conditions for Q -He collisions stochastically based on this energy within the ergodic approximation, before enacting a billiard-ball elastic collision and tracking the change to the energy after the collision, which is again stored, and so on. This is numerically efficient, since no trajectories need to be integrated to simulate the dynamics. The simulations rely on the ergodic approximation, valid when the orbits in the trap are fast compared to the mean Q -He collision time. The simulations also assume the Q density is small compared to the He density, so Q -He collisions need to be considered but Q - Q collisions can be mostly ignored. In all collisions, the small effect of the trap light on the buffer gas atoms is ignored. We also approximate all collisions as equally likely to occur at all times so that the ergodic theorem is relevant for drawing initial conditions, even though, as in Sec. VA, collisions are technically more likely to occur at times of Q ’s motion where its speed is higher.

In our simulations, we approximate the trap potential of a single lattice site j as a truncated harmonic potential,

$$U(\mathbf{x}; j) \approx \min \left[\left(-\eta(j)k_B T + \sum_{i=1}^3 \frac{1}{2} m_Q \omega_i^2(j) x_i^2 \right), 0 \right], \quad (\text{C1})$$

in order to efficiently sample initial conditions for collisions from the energy hypersurfaces. Here, the ω_i represent the trap angular frequencies $\omega_x = \omega_y = \sqrt{4\eta(j)k_B T / m_Q w(j)^2} = \omega_r$ and $\omega_z = \sqrt{8\pi^2 \eta(j)k_B T / m_Q \lambda^2}$. We also ignore the constraint that orbits in the trap conserve the z component of angular momentum. We stress that we are still making the ergodic approximation, we are simply taking initial conditions for collisions from a simpler physical system than the fully nonlinear trapping potential. The simulation volume for lattice site j , centered on the antinode at z_j , is defined as the region where the approximate trap potential in Eq. (C1) is nonzero, and consists of an ellipsoid with volume $V_e(z_j) = w^2(z_j)\lambda/3$, assuming the lattice site is near the trap center where wavefront curvature can be ignored.

In action-angle coordinates, sampling from the energy hypersurface amounts to drawing three random angle variables and three random actions J_i under the constraint that $E + \eta k_B T = \sum_{i=1}^3 \omega_i J_i$. This is efficiently done by drawing two random numbers between 0 and 1 and using them as a partition of the interval into three randomly drawn pieces. These are translated back to regular phase-space coordinates to draw initial conditions for bound Q molecules in collisions.

There are two forms of the ergodic loading simulations, namely, that which computes the loading fractions f_i , and that which computes the mean number of Q -He collisions needed to eject a trapped molecule, $k_{Q\text{-He}}$, which are discussed in Sec. V B 2. The results of both are required to construct the loading model in Sec. V B 3. For the simulation of the loading fractions f_i , an untrapped Q molecule is first spawned randomly in the simulation volume. Its velocity is drawn from a Maxwell distribution at the buffer gas temperature $T = 1.5$ K and its position \mathbf{x} is drawn uniformly within the simulation volume, before its kinetic energy is increased due to the local trap potential $U(\mathbf{x})$. Its speed is computed as $v = \sqrt{2(E - U)/m_Q}$, and its direction is randomized. The initial condition for a first billiard-ball collision is now set by drawing a buffer gas atom from a Maxwell distribution at T . If the molecule is bound by the collision, only its energy needs to be retained, since before every subsequent collision new initial conditions are drawn by randomly sampling the energy hypersurface within the ergodic approximation. There is no need to integrate the Q trajectory. The simulation continues until Q 's energy either becomes positive and the molecule escapes, or it stays negative and falls below the energy of a molecule drawn from a Boltzmann distribution in the trap at T .

For the simulation of the number of Q -He collisions needed to eject a trapped molecule, $k_{Q\text{-He}}$, a molecule is initially drawn with an energy from a Boltzmann distribution within the trap, and with phase-space coordinates drawn ergodically from the corresponding energy hypersurface. Billiard-ball collisions are repeatedly enacted with buffer gas atoms until the molecule is eventually ejected from the trap ($E > 0$), giving $k_{Q\text{-He}}$.

APPENDIX D: TRAP HEATING CAUSED BY LASER NOISE

Laser noise can cause trap heating in two ways [174,175]. Firstly, laser intensity noise (RIN) at twice the trap angular frequencies $\omega_r = 2\pi \times 2$ MHz and $\omega_z = 2\pi \times 68$ MHz lead to parametric driving of trapped molecules, resulting in a heating rate Γ^{RIN} at which energy grows exponentially in the trap:

$$\Gamma_i^{\text{RIN}} = \frac{1}{4} \omega_i^2 S_\epsilon(2\omega_i), \quad (\text{D1})$$

where $S_\epsilon(\omega)$ is the one-sided power spectrum (in units of dBc/Hz) of the relative intensity noise $\Delta I/I$ at an angular frequency ω [174].

We have measured the RIN of our laser oscillator (NKT Koheras Adjustik Y10) to be -147 dBc/Hz (-154 dBc/Hz) at 4 MHz (136 MHz), which corresponds to $\Gamma_r^{\text{RIN}} = 8 \times 10^{-2} \text{ s}^{-1}$ ($\Gamma_z^{\text{RIN}} = 18 \text{ s}^{-1}$). However, the cavity acts as a frequency filter with, for perfect spatial mode matching, the normalized transfer function $|G(\omega)|^2 = (\pi^2/2\mathcal{F}^2)/(1 - \cos(2\pi f/\text{FSR}))$ (for $\mathcal{F} \gg 1$ and $|f - N \text{FSR}| \gg \Delta\nu$, $N = 0, 1, \dots$), where f is the frequency offset from the frequency resonant with the cavity, \mathcal{F} is the cavity's finesse, and L is its length, and $\text{FSR} = c/2L$ and $\Delta\nu = \text{FSR}/\mathcal{F}$ are the cavity's resulting free spectral range and linewidth, respectively. RIN at frequency f , which corresponds to amplitude modulation at f , is thus further suppressed. At $f = 2\omega_r/2\pi$ ($f = 2\omega_z/2\pi$), this results in a suppression by 46 dB (76 dB), and a resulting $\Gamma_r^{\text{RIN}} \approx 2 \times 10^{-6} \text{ s}^{-1}$ ($\Gamma_z^{\text{RIN}} \approx 5 \times 10^{-7} \text{ s}^{-1}$), assuming the measured RIN values outside the cavity. We note that the value of Γ_z^{RIN} is within a factor of two of the shot-noise of the circulating power inside the cavity. We also note that imperfect spatial mode matching will reduce the cavity's suppression. In particular, $2\omega_r = 2\pi \times 4$ MHz is close to the difference in resonance frequencies of $\Delta f_{10} = 3.6$ MHz between the $\text{TEM}_{01}/\text{TEM}_{10}$ modes and the fundamental TEM_{00} mode. Finally, we do not expect that the high-power fiber amplifier to be used in the experiment adds substantial RIN at the frequencies of interest.

Secondly, movement of the trap center by an amount $\mathbf{x}(t)$ results in a linear growth in average energy,

$$\langle \dot{E} \rangle_i = \frac{\pi}{2} m_Q \omega_i^4 S_x(\omega_i), \quad (\text{D2})$$

which now could lead to significant heating due to the quartic dependence on the trap frequency. Here, S_x is the one-sided power spectrum of position fluctuations in the trap center [174]. However, we expect acoustic noise at MHz frequencies to be sufficiently small.

APPENDIX E: TWO-BODY LOSS MODELS

1. Universal loss

In optical trapping experiments on alkali molecules, two-body loss is a result of so-called "universal loss", in which a large fraction of collisions between trapped molecules lead to loss. One argument suggests that our trap will not experience universal loss. In this argument, the loss mechanism involves strong perturbation of molecular energy levels by a partner, which leads to an excited state of the two-body complex located one photon energy of the trap light above the ground

state [176]. For long enough lifetimes of the complex, the probability to reach this excited state, causing subsequent loss of the molecules, then approaches unity. However, the interactions between SCS molecules are often of order 20 meV [177,178], which is two orders of magnitude too small to perturb the excited states by several eV and unlock a single-photon excitation of the complex. Moreover, the complex lifetimes of SCS molecules (based on a semiclassical model presented in Ref. [153]) are only of order picoseconds, so the notion of “sticky molecular collisions” seems inapplicable to our trap. Hence, one expects not to see universal loss for Q .

However, recent literature has cast some doubt over this explanation [129]. Therefore we consider a worst-case scenario in which universal loss occurs for all Q - Q collisions in the trap. This worst-case scenario provides an upper bound for the two-body loss rates expected from general two-body loss processes that are difficult to estimate in the cold, high-intensity conditions of our trap. We do not, however, treat Q -He collisions as lossy, as the interactions are only $O(5 \text{ meV})$ [126].

In universal loss, the functional form of the two-body loss coefficient β_{Q-Q} depends on whether or not an s -wave two-body interaction is allowed, which in turn depends on whether the molecules can be regarded as indistinguishable and Bosonic. Since the s -wave loss rates are higher than the p -wave loss rates, we must assume in a worst-case estimate that we will be limited by s -wave scattering, in which [179]

$$\beta_{Q-Q} = 4\pi \frac{\hbar}{\mu} a, \quad (\text{E1})$$

where the Van der Waals length a is here defined by the C_6 coefficient through $a = 0.4778(2\mu C_6/\hbar^2)^{1/4}$ [180], and μ is the reduced mass of the two bodies.

For many small molecules, a typical value of C_6 is a few tens to hundreds of atomic units ($E_h a_0^6$), and the $C_6^{1/4}$ dependence of β_{Q-Q} means a good estimate is not critical. Using C_6 coefficients from an approximate formula in [181], we obtain, including an extra factor of two as noted in [179], values of β_{Q-Q} slightly less than $1 \times 10^{-10} \text{ cm}^3/\text{s}$ for many molecules, and assign $\beta_{Q-Q} = 10^{-10} \text{ cm}^3/\text{s}$ for Q , which is consistent with typical values in [179]. In the main text, we keep in mind the strong likelihood that universal loss does not occur for Q , in which case two-body losses may not limit the trapped density. By experimentally observing the two-body loss rate for molecules in our trap, we will be able to provide useful insight into the nature of cold collisions and the mechanism of universal loss.

2. Collision-induced absorption

In high-density gases, optical transitions that are forbidden for single molecules can become allowed through collision-induced absorption (CIA) [182]. To our knowledge, of the molecules in Table I, only O_2 exhibits CIA at 1064 nm. From Fig. 1(b) of Ref. [183], the absorption of this feature is $\alpha_{\text{CIA}} = 10^{-6} \text{ cm}^{-1} \text{ am}^{-2} = 1.39 \times 10^{-45} \text{ cm}^5/\text{molecule}^2$. Assuming every CIA event leads to loss, the resulting two-body loss coefficient is $\beta = \alpha_{\text{CIA}} I/\hbar\omega = 2.2 \times 10^{-15} \text{ cm}^3/\text{s}$, which is small compared to other two-body loss coefficients considered in Fig. 6. It therefore appears that even in the worst case of CIA features centered at 1064 nm, the densities required to induce absorption are high compared to those we expect to see

in our experiment. CIA effects can therefore be ignored in our experiment.

APPENDIX F: TRAP HEATING AND LOSS FROM ROTATIONAL RAMAN SCATTERING

Here, we compute the rotational Raman scattering (RSS) loss term Γ_{RR} of Eq. (7). RRS from the $J = 0$ rotational ground state to the $J = 2$ excited state increases a molecule's internal energy by $\Delta E_{\text{RR}} = 6B$, which is $\sim 15 \text{ K}$, and hence greater than T_{trap} , for many molecules in Table I. Rotationally inelastic collisions typically occur once per ~ 10 elastic collisions [123], which is 10^4 s^{-1} , much faster than RRS rates in Table I. We therefore assume molecules are only rotationally excited once before being immediately rotationally cooled to the ground state, whereby their rotational energy is converted to translational kinetic energy.

In $Q(J = 2)$ - $Q(J = 0)$ inelastic collisions, which occur at a rate $\nu_{Q-Q,i}$, on average ΔE_{RR} is split evenly between the molecules, so most likely a molecule will be ejected from the trap. On the other hand, in $Q(J = 2)$ -He inelastic collisions, which occur at a rate $\nu_{Q-\text{He},i}$, only $\mu/m_Q = 1/8.5$ of ΔE_{RR} goes to the molecule's translational energy, the rest being carried away by the much lighter He atom. Therefore, while the fraction $\nu_{Q-Q,i}/(\nu_{Q-\text{He},i} + \nu_{Q-Q,i})$ of RRS events simply lead to loss, the remaining fraction $\nu_{Q-\text{He},i}/(\nu_{Q-\text{He},i} + \nu_{Q-Q,i})$ do not. They instead lead to heating of the sample of N trapped molecules, increasing the total kinetic and potential energy of the trapped sample at a rate $\dot{E}_h = \frac{\mu}{m_Q} \Delta E_{\text{RR}} W_{\text{RR}} N$. This heating will lead to some molecule loss, which we can bound above by assuming, conservatively, that the buffer-gas cooling does not compensate for \dot{E}_h at all, and the heat is instead balanced exclusively by molecule loss. Every time a thermalized molecule is lost from the trapped sample, it carries away on average $(\eta + \kappa - 3)k_B T$ of energy ($\kappa = (1 - \Gamma(5, \eta))/(\eta\Gamma(3, \eta) - 4\Gamma(4, \eta))$, where Γ is the incomplete Gamma function [134]). Balancing \dot{E}_h with this loss and combining with the $Q(J = 2)$ - $Q(J = 0)$ case, an upper bound for the overall loss rate due to RRS is

$$\Gamma_{\text{RR}} = - \frac{\nu_{Q-\text{He},i}}{\nu_{Q-\text{He},i} + \nu_{Q-Q,i}} \frac{(\mu/m_Q)\Delta E_{\text{RR}}W_{\text{RR}}N}{(\eta + \kappa - 3)k_B T} - \frac{\nu_{Q-Q,i}}{\nu_{Q-\text{He},i} + \nu_{Q-Q,i}} W_{\text{RR}}N. \quad (\text{F1})$$

This loss term has a nonlinear dependence on N as $\nu_{Q-Q,i}$ depends on the trapped density.

To evaluate Eq. (F1), inelastic collision cross sections are required. For N_2 [Fig. 6(d)], we approximate He- N_2 inelastic collision cross sections using the elastic cross section from [125] and the inelastic-to-elastic collision ratio from [184], and we take the N_2 - N_2 inelastic collision cross sections from [185,186]. We estimate the inelastic N_2 - N_2 and N_2 -He cross sections at 1.5 K to be 100 and 40 \AA^2 , respectively.

APPENDIX G: LASER-INDUCED BREAKDOWN

Laser-induced breakdown occurs when an electron created in the laser beam, for instance by multiphoton ionization (MPI), is heated by inverse bremsstrahlung in collisions with neighboring molecules to above the ionization energy of a

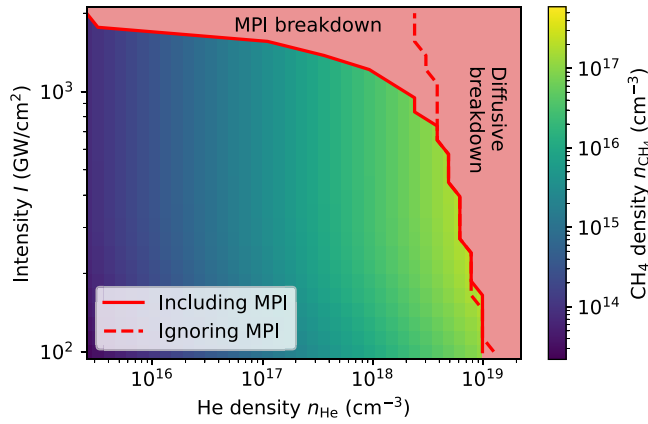


FIG. 7. Laser-induced breakdown simulations. Simulations determine when one electron spawned in the beam creates more than one electron in the laser beam before it diffuses out. The solid curve includes electrons created independently through multiphoton ionization (MPI) before the electron diffusion out of the beam. The dashed curve ignores these electrons and purely counts electrons formed by impact ionization. The red-filled region is that bounded below by the solid curve, indicating the region where breakdown occurs. Inset are the CH_4 densities used in the simulation, which are taken from the steady state of Eq. (7), despite the fact that the model is not strictly valid at the comparatively high densities used in this simulation. Here, we fix $n_{\text{CH}_4, \text{LR}}/n_{\text{He}} = 1/100$ and assume universal loss in Eq. (7). Our conclusions on breakdown are not sensitive to these choices.

molecule, so it can free new electrons by impact ionization. This can lead to exponential growth in the electron number. The process is well understood in high-intensity, pulsed lasers and at high gas densities [104,187–191]. However, the treatment of breakdown in continuous-wave (CW) laser beams is often left as an afterthought, because CW intensities are rarely high enough to induce breakdown.

Fortunately, the theory of breakdown in CW laser beams is straightforward. In this case, breakdown can be treated as an electron diffusion problem: breakdown occurs when an electron spawns in the beam and causes more than one ionization event before it leaves. Once outside the beam, the electrons will cool down rather than be collisionally heated, and eventually recombine with ions, and so will no longer contribute to further ionization events. We do not consider the ion motion as contributing to breakdown, because the collisional heating rate of the ions is suppressed by their much higher mass.

At the relatively low buffer gas densities we are interested in, macroscopic treatments of breakdown [189] are not required, and it is instead numerically tractable to simulate entire electron trajectories through the laser beam. Electrons are spawned at the center of the beam in the radial direction, and within a Rayleigh range of the focus in the axial direction. Based on Ref. [187], their initial energies are drawn from a Boltzmann distribution with mean energy $I_0/3$, I_0 being the He ionization energy. For self-consistency, we have confirmed in our simulations that electrons formed from impact ionization events at intensities of order 100 GW/cm^2 have roughly this energy. The electron motion is modeled stepwise, with step

sizes drawn from an exponential distribution of mean size l_e , where l_e is the electron mean free path, computed as

$$\frac{1}{l_e} = \sum_{\text{gas } i} \sum_{\text{process } j} n_i \sigma_{ij}, \quad (\text{G1})$$

where i indexes between Q and He, n_i represent the gas number densities, and σ_{ij} is the cross section for electron collisions with gas i that lead to process j . The gas densities are taken to be consistent with Eq. (7) during the loading phase, and we assume there is no ion density, as electron multiplication begins before there is a large number of ions in the beam. The processes we consider are elastic collisions, electronically exciting collisions, and ionizing collisions. Exciting collisions are counted as ionizing collisions as the trap light would likely ionize any electronically excited molecule. In each case, we treat the gas particles as stationary targets due to their much lower velocity, and model the cross sections as spherically symmetric for simplicity.

In each collision, a number of photons may be absorbed due to inverse bremsstrahlung, which modifies the cross sections. For an exciting or elastic process with a laser-free cross section $\sigma_{E_1 \rightarrow E_2}^{(0)}(E_1)$, the cross section is modified to [192–195]

$$\begin{aligned} \sigma_{E_1 \rightarrow E_2}^{(0)}(E_1) &\rightarrow \sum_{n=-\infty}^{\infty} \sigma_{E_1 \rightarrow E_2}^{(n)} \\ &= \sum_{n=-\infty}^{\infty} \sigma_{E_1 + n\hbar\omega \rightarrow E_2}^{(0)}(E_1 + n\hbar\omega) \\ &\quad \times \sqrt{1 + \frac{n\hbar\omega}{E_1} J_n^2 \left(\frac{eE_0}{m_e \omega^2} |\Delta k_x| \right) \Big|_{E_2 = E_1 + n\hbar\omega > 0}}, \quad (\text{G2}) \end{aligned}$$

where n represents the number of photons absorbed in the process, e the electron charge, E_0 the electric field amplitude, m_e the electron mass, ω the optical angular frequency, J_n the n th-order Bessel function of the first kind, and Δk_x the change (along the axis of optical polarization, here the x axis) in the electron's \mathbf{k} vector in the collision. We do not modify cross sections in which a third body is created in this way.

In our simulations, we use a particular target, CH_4 , to represent Q , because electron-impact cross section data is difficult to choose for Q . The energy-dependent, laser-free cross sections for helium are compiled from Refs. [196] (elastic), [197] (exciting), and [198] (ionizing). CH_4 cross sections are taken from Song [199], except for dissociation cross sections (which we take to be inelastic but not ionizing) which are found in Ref. [200] and multiplied by 2 to fit with Song's sparsely populated but likely more accurate data. The binary encounter dipole model (Ref. [201] for helium and Ref. [202] for methane) is used to draw electron velocities after impact ionization events to continue their trajectories. Other molecules, like N_2 and O_2 , have similar orders of magnitude for their electron-impact cross sections [203,204], so we believe that our conclusions for breakdown in a mostly helium He- CH_4 mixture will generalize to other species we would like to trap.

One challenge with using these cross sections is that l_e depends on the local light intensity and gas density. One would need to update l_e depending on where the electron moves

in one step, which is itself determined by l_e . We overcome this using a “feedforward” method, in which l_e is determined by the local intensity and densities at the previous step. We expect this to only cause small errors, and this approximation is needed to make the problem tractable.

Armed with the relevant cross sections, at each step of mean distance l_e and random direction, we stochastically decide which process occurs and how many photons are absorbed with relative weights $n_i \sigma_{ij}^{(n)}$. From the chosen process, we update the electron energy, and count whether an ionization event has occurred. We also update the electron energy by the ponderomotive potential, which causes minimal change to the simulation results. We stop an electron’s simulation when it has moved three waists from the beam’s central axis. We also track the total time taken for the electron to diffuse, and we can add electrons spawned from multiphoton ionization (MPI) during this time to compute the breakdown condition when MPI is included. We count how many electrons are created from each electron we spawned, and if this

number is greater than one, we decide that breakdown has occurred.

The results are shown in Fig. 7. It is known that in the diffusive breakdown regime, the intensity threshold I_{th} depends on the gas pressure p as [190]

$$I_{th} \sim p^{-2/m'}, \quad (G3)$$

where m' is a constant near 1. For breakdown dominated by MPI instead of electron diffusion, this constant m' becomes quite large, and the pressure dependence becomes small. We can see both of these regimes in Fig. 7. When MPI electrons are ignored, there is a strong dependence on pressure, but when they are added, I_{th} becomes a slow-varying function of pressure at high enough intensities. Breakdown appears to occur at densities and intensities much higher than we will require, so it will not limit our experiment.

-
- [1] H. Metcalf and P. van der Straten, *Laser Cooling and Trapping*, Graduate Texts in Contemporary Physics (Springer, New York, 2001).
- [2] L. Postler, S. Heußen, I. Pogorelov, M. Rispler, T. Feldker, M. Meth, C. D. Marciniak, R. Stricker, M. Ringbauer, R. Blatt, P. Schindler, M. Müller, and T. Monz, Demonstration of fault-tolerant universal quantum gate operations, *Nature* **605**, 675 (2022).
- [3] I. Bloch, J. Dalibard, and S. Nascimbène, Quantum simulations with ultracold quantum gases, *Nat. Phys.* **8**, 267 (2012).
- [4] M. Lewenstein, A. Sanpera, and V. Ahufinger, *Ultracold Atoms in Optical Lattices: Simulating Quantum Many-Body Systems* (Oxford University Press, Oxford, UK, 2012).
- [5] A. D. Ludlow, M. M. Boyd, J. Ye, E. Peik, and P. O. Schmidt, Optical atomic clocks, *Rev. Mod. Phys.* **87**, 637 (2015).
- [6] R. H. Parker, C. Yu, W. Zhong, B. Estey, and H. Müller, Measurement of the fine-structure constant as a test of the Standard Model, *Science* **360**, 191 (2018).
- [7] R. Krems, W. C. Stwalley, and B. Friedrich, *Cold molecules: Theory, Experiment, Applications* (CRC Press, Boca Raton, 2009).
- [8] B. Friedrich and J. M. Doyle, Why are cold molecules so hot? *ChemPhysChem* **10**, 604 (2009).
- [9] D. DeMille, Quantum Computation with Trapped Polar Molecules, *Phys. Rev. Lett.* **88**, 067901 (2002).
- [10] V. V. Albert, J. P. Covey, and J. Preskill, Robust Encoding of a Qubit in a Molecule, *Phys. Rev. X* **10**, 031050 (2020).
- [11] J. L. Bohn, A. M. Rey, and J. Ye, Cold molecules: Progress in quantum engineering of chemistry and quantum matter, *Science* **357**, 1002 (2017).
- [12] L. Santos, G. V. Shlyapnikov, P. Zoller, and M. Lewenstein, Bose-Einstein Condensation in Trapped Dipolar Gases, *Phys. Rev. Lett.* **85**, 1791 (2000).
- [13] L. De Marco, G. Valtolina, K. Matsuda, W. G. Tobias, J. P. Covey, and J. Ye, A degenerate Fermi gas of polar molecules, *Science* **363**, 853 (2019).
- [14] M. S. Safronova, D. Budker, D. DeMille, D. F. J. Kimball, A. Derevianko, and C. W. Clark, Search for new physics with atoms and molecules, *Rev. Mod. Phys.* **90**, 025008 (2018).
- [15] ACME Collaboration, Improved limit on the electric dipole moment of the electron, *Nature* **562**, 355 (2018).
- [16] W. B. Cairncross and J. Ye, Atoms and molecules in the search for time-reversal symmetry violation, *Nat. Rev. Phys.* **1**, 510 (2019).
- [17] N. Balakrishnan, Perspective: Ultracold molecules and the dawn of cold controlled chemistry, *J. Chem. Phys.* **145**, 150901 (2016).
- [18] B. R. Heazlewood and T. P. Softley, Towards chemistry at absolute zero, *Nat. Rev. Chem.* **5**, 125 (2021).
- [19] C. Puzzarini, Grand challenges in astrochemistry, *Front. Astron. Space Sci.* **7**, 19 (2020).
- [20] D. R. Herschbach, Molecular dynamics of elementary chemical reactions (Nobel lecture), *Angew. Chem., Int. Ed. Engl.* **26**, 1221 (1987).
- [21] Y. T. Lee, Molecular beam studies of elementary chemical processes (Nobel lecture), *Angew. Chem., Int. Ed. Engl.* **26**, 939 (1987).
- [22] R. A. Phaneuf, C. C. Havener, G. H. Dunn, and A. Müller, Merged-beams experiments in atomic and molecular physics, *Rep. Prog. Phys.* **62**, 1143 (1999).
- [23] W. C. Campbell and J. M. Doyle, Cooling, trap loading, and beam production using a cryogenic helium buffer gas, *Cold Molecules: Theory, Experiment, Applications* (CRC Press, Boca Raton, FL, 2009), pp. 473–508.
- [24] B. Spaun, P. B. Changala, D. Patterson, B. J. Bjork, O. H. Heckl, J. M. Doyle, and J. Ye, Continuous probing of cold complex molecules with infrared frequency comb spectroscopy, *Nature* **533**, 517 (2016).
- [25] P. B. Changala, B. Spaun, D. Patterson, J. M. Doyle, and J. Ye, Sensitivity and resolution in frequency comb spectroscopy of buffer gas cooled polyatomic molecules, *Appl. Phys. B* **122**, 292 (2016).

- [26] J. D. Weinstein, R. deCarvalho, T. Guillet, B. Friedrich, and J. M. Doyle, Magnetic trapping of calcium monohydride molecules at millikelvin temperatures, *Nature* **395**, 148 (1998).
- [27] W. C. Campbell, E. Tsikata, H.-I. Lu, L. D. van Buuren, and J. M. Doyle, Magnetic Trapping and Zeeman Relaxation of $\text{NH } \lambda^3\sigma^-$, *Phys. Rev. Lett.* **98**, 213001 (2007).
- [28] Y. Segev, M. Pitzer, M. Karpov, N. Akerman, J. Narevicius, and E. Narevicius, Collisions between cold molecules in a superconducting magnetic trap, *Nature* **572**, 189 (2019).
- [29] R. Wild, M. Nötzold, C. Lochmann, and R. Wester, Complex formation in three-body reactions of Cl^- with H_2 , *J. Phys. Chem. A* **125**, 8581 (2021).
- [30] F. A. Gianturco, K. Giri, L. Gonzalez-Sanchez, E. Yurtsever, N. Sathyamurthy, and R. Wester, Efficiency of rovibrational cooling of HeH^+ by collisions with He: Cross sections and rate coefficients from quantum dynamics, *J. Chem. Phys.* **155**, 154301 (2021).
- [31] H. L. Bethlem, G. Berden, F. M. H. Crompvoets, R. T. Jongma, A. J. A. van Rooij, and G. Meijer, Electrostatic trapping of ammonia molecules, *Nature* **406**, 491 (2000).
- [32] S. Y. T. van de Meerakker, P. H. M. Smeets, N. Vanhaecke, R. T. Jongma, and G. Meijer, Deceleration and Electrostatic Trapping of OH Radicals, *Phys. Rev. Lett.* **94**, 023004 (2005).
- [33] A. Prehn, M. Ibrügger, R. Glöckner, G. Rempe, and M. Zeppenfeld, Optoelectrical Cooling of Polar Molecules to Submillikelvin Temperatures, *Phys. Rev. Lett.* **116**, 063005 (2016).
- [34] D. DeMille, D. R. Glenn, and J. Petricka, Microwave traps for cold polar molecules, *Eur. Phys. J. D* **31**, 375 (2004).
- [35] S. C. Wright, T. E. Wall, and M. R. Tarbutt, Microwave trap for atoms and molecules, *Phys. Rev. Res.* **1**, 033035 (2019).
- [36] S. Moses, J. Covey, M. Miccnikowski, D. Jin, and J. Ye, New frontiers for quantum gases of polar molecules, *Nat. Phys.* **13**, 13 (2017).
- [37] Y. Liu, M.-G. Hu, M. A. Nichols, D. D. Grimes, T. Karman, H. Guo, and K.-K. Ni, Photo-excitation of long-lived transient intermediates in ultracold reactions, *Nat. Phys.* **16**, 1132 (2020).
- [38] P. D. Gregory, J. A. Blackmore, S. L. Bromley, J. M. Hutson, and S. L. Cornish, Robust storage qubits in ultracold polar molecules, *Nat. Phys.* **17**, 1149 (2021).
- [39] D. Mitra, N. B. Vilas, C. Hallas, L. Anderegg, B. L. Augenbraun, L. Baum, C. Miller, S. Raval, and J. M. Doyle, Direct laser cooling of a symmetric top molecule, *Science* **369**, 1366 (2020).
- [40] E. S. Shuman, J. F. Barry, and D. DeMille, Laser cooling of a diatomic molecule, *Nature* **467**, 820 (2010).
- [41] L. Anderegg, B. L. Augenbraun, Y. Bao, S. Burchesky, L. W. Cheuk, W. Ketterle, and J. M. Doyle, Laser cooling of optically trapped molecules, *Nat. Phys.* **14**, 890 (2018).
- [42] L. Baum, N. B. Vilas, C. Hallas, B. L. Augenbraun, S. Raval, D. Mitra, and J. M. Doyle, 1D Magneto-Optical Trap of Polyatomic Molecules, *Phys. Rev. Lett.* **124**, 133201 (2020).
- [43] S. Ding, Y. Wu, I. A. Finneran, J. J. Bureau, and J. Ye, Sub-Doppler Cooling and Compressed Trapping of YO Molecules at μK Temperatures, *Phys. Rev. X* **10**, 021049 (2020).
- [44] J. Lim, J. R. Almond, M. A. Trigatzis, J. A. Devlin, N. J. Fitch, B. E. Sauer, M. R. Tarbutt, and E. A. Hinds, Laser Cooled YbF Molecules for Measuring the Electron's Electric Dipole Moment, *Phys. Rev. Lett.* **120**, 123201 (2018).
- [45] I. Kozyryev, L. Baum, K. Matsuda, B. L. Augenbraun, L. Anderegg, A. P. Sedlack, and J. M. Doyle, Sisyphus Laser Cooling of a Polyatomic Molecule, *Phys. Rev. Lett.* **118**, 173201 (2017).
- [46] B. L. Augenbraun, Z. D. Lasner, A. Frenett, H. Sawaoka, C. Miller, T. C. Steimle, and J. M. Doyle, Laser-cooled polyatomic molecules for improved electron electric dipole moment searches, *New J. Phys.* **22**, 022003 (2020).
- [47] R. L. McNally, I. Kozyryev, S. Vazquez-Carson, K. Wenz, T. Wang, and T. Zelevinsky, Optical cycling, radiative deflection and laser cooling of barium monohydride ($^{138}\text{Ba}^1\text{H}$), *New J. Phys.* **22**, 083047 (2020).
- [48] N. Fitch and M. Tarbutt, Laser-cooled molecules, in *Advances In Atomic, Molecular, and Optical Physics* (Academic Press, Cambridge, MA, 2021), Vol. 70, pp. 157–262.
- [49] B. Friedrich and D. Herschbach, Alignment and Trapping of Molecules in Intense Laser Fields, *Phys. Rev. Lett.* **74**, 4623 (1995).
- [50] C. Turnbaugh, J. J. Axelrod, S. L. Campbell, J. Y. Dioquino, P. N. Petrov, J. Remis, O. Schwartz, Z. Yu, Y. Cheng, R. M. Glaeser, and H. Mueller, High-power near-concentric Fabry-Pérot cavity for phase contrast electron microscopy, *Rev. Sci. Instrum.* **92**, 053005 (2021).
- [51] O. Schwartz, J. J. Axelrod, S. L. Campbell, C. Turnbaugh, R. M. Glaeser, and H. Müller, Laser phase plate for transmission electron microscopy, *Nat. Methods* **16**, 1016 (2019).
- [52] O. Schwartz, J. Axelrod, D. R. Tuthill, P. Haslinger, C. Ophus, R. Glaeser, and H. Müller, Near-concentric Fabry-Pérot cavity for continuous-wave laser control of electron waves, *Opt. Express* **25**, 14453 (2017).
- [53] NIST Computational Chemistry Comparison and Benchmark Database, editor: Russell D. Johnson III, NIST Standard Reference Database Number 101. Release 22, May 2022.
- [54] NIST Chemistry WebBook: NIST Standard Reference Database Number 69 (2021).
- [55] The HIGH-resolution TRANsmision (HITRAN) database (2021). Atomic and Molecular Physics Division, Harvard-Smithsonian Center for Astrophysics.
- [56] H. Keller-Rudek, G. K. Moortgat, R. Sander, and R. Sörensen, The MPI-Mainz UV/VIS spectral atlas of gaseous molecules of atmospheric interest, *Earth System Science Data* **5**, 365 (2013).
- [57] N. J. Bridge, A. D. Buckingham, and J. W. Linnett, The polarization of laser light scattered by gases, *Proc. R. Soc. London A* **295**, 334 (1966).
- [58] M. P. Bogaard, A. D. Buckingham, R. K. Pierens, and A. H. White, Rayleigh scattering depolarization ratio and molecular polarizability anisotropy for gases, *J. Chem. Soc., Faraday Trans. 1* **74**, 3008 (1978).
- [59] S. McGuire and R. Miles, Collision induced ultraviolet structure in nitrogen radar REMPI spectra, *J. Chem. Phys.* **141**, 244301 (2014).
- [60] W. X. Peng, K. W. D. Ledingham, and R. P. Singhal, Trace CO detection by REMPI at 230 nm, *AIP Conf. Proc.* **388**, 219 (1997).
- [61] R. J. Yokelson, R. J. Lipert, and W. A. Chupka, Identification of the $n\sigma$ and $nd\lambda$ Rydberg states of O_2 for $n=3-5$, *J. Chem. Phys.* **97**, 6153 (1992).
- [62] D. S. Green, G. A. Bickel, and S. C. Wallace, $(2+1)$ resonance enhanced multiphoton ionization of hydrogen chloride in a

- pulsed supersonic jet: Spectroscopic survey, *J. Mol. Spectrosc.* **150**, 303 (1991).
- [63] C. A. Galea, M. N. Shneider, M. Gragston, and Z. Zhang, Coherent microwave scattering from xenon resonance-enhanced multiphoton ionization-initiated plasma in air, *J. Appl. Phys.* **127**, 053301 (2020).
- [64] W. Zernik, Two-photon ionization of atomic hydrogen, *Phys. Rev.* **135**, A51 (1964).
- [65] E. E. Marinero, C. T. Rettner, and R. N. Zare, Quantum-State-Specific Detection of Molecular Hydrogen by Three-Photon Ionization, *Phys. Rev. Lett.* **48**, 1323 (1982).
- [66] D. P. Taylor and P. M. Johnson, Resonance enhanced multiphoton ionization photoelectron spectra of CO₂. III. Autoionization dominates direct ionization, *J. Chem. Phys.* **98**, 1810 (1993).
- [67] T. F. Hanisco and A. C. Kummel, State-resolved photodissociation of nitrous oxide, *J. Phys. Chem.* **97**, 7242 (1993).
- [68] M. S. N. Al-Kahali, R. J. Donovan, K. P. Lawley, and T. Ridley, Mass-resolved multiphoton ionization spectroscopy of jet-cooled Cl₂. II. The (2+1) REMPI spectrum between 76000 and 90000 cm⁻¹, *J. Chem. Phys.* **104**, 1833 (1996).
- [69] Z. Hu, W.-B. Lee, X.-P. Zhang, P.-Y. Wei, and K.-C. Lin, (1+1) resonance-enhanced multiphoton ionization and photodissociation study of CS₂ via the ²B₂ state, *ChemPhysChem* **9**, 422 (2008).
- [70] R. Fulton, A. I. Bishop, M. N. Shneider, and P. F. Barker, Controlling the motion of cold molecules with deep periodic optical potentials, *Nat. Phys.* **2**, 465 (2006).
- [71] E. J. Salumbides, A. Khramov, and W. Ubachs, High-Resolution 2 + 1 REMPI Study of the a¹Σ_g⁺ State in N₂, *J. Phys. Chem. A* **113**, 2383 (2009).
- [72] J. J. Axelrod, S. L. Campbell, O. Schwartz, C. Turnbaugh, R. M. Glaeser, and H. Müller, Observation of the Relativistic Reversal of the Ponderomotive Potential, *Phys. Rev. Lett.* **124**, 174801 (2020).
- [73] S. Truppe, M. Hambach, S. M. Skoff, N. E. Bulleid, J. S. Bumby, R. J. Hendricks, E. A. Hinds, B. E. Sauer, and M. R. Tarbutt, A buffer gas beam source for short, intense and slow molecular pulses, *J. Mod. Opt.* **65**, 648 (2018).
- [74] L. G. Anderegg, Ultracold molecules in optical arrays: From laser cooling to molecular collisions, Ph.D. thesis, Harvard University, 2019.
- [75] L. W. Baum, Laser cooling and 1D magneto-optical trapping of calcium monohydroxide, Ph.D. thesis, Harvard University, 2020.
- [76] Y. Takahashi, D. Shlivko, G. Woolls, and N. R. Hutzler, Simulation of cryogenic buffer gas beams, *Phys. Rev. Res.* **3**, 023018 (2021).
- [77] C. Day, Basics and applications of cryopumps, *CAS - CERN Accelerator School: Vacuum Accelerators*, 241 (2007).
- [78] N. B. Vilas, C. Hallas, L. Anderegg, P. Robichaud, A. Winnicki, D. Mitra, and J. M. Doyle, Magneto-optical trapping and sub-Doppler cooling of a polyatomic molecule, *Nature* **606**, 70 (2022).
- [79] T. Takekoshi, J. Yeh, and R. Knize, Quasi-electrostatic trap for neutral atoms, *Opt. Commun.* **114**, 421 (1995).
- [80] T. Takekoshi and R. J. Knize, CO₂ laser trap for cesium atoms, *Opt. Lett.* **21**, 77 (1996).
- [81] H. Engler, A quasi-electrostatic trap for neutral atoms, Ph.D. thesis, University of Heidelberg, 2000.
- [82] R. Grimm, M. Weidemüller, and Y. B. Ovchinnikov, Optical dipole traps for neutral atoms, in *Advances In Atomic, Molecular, and Optical Physics*, Vol. 42, edited by B. Bederson and H. Walther (Academic Press, Cambridge, MA, 2000), pp. 95–170.
- [83] F. Le Kien, P. Schneeweiss, and A. Rauschenbeutel, Dynamical polarizability of atoms in arbitrary light fields: general theory and application to cesium, *Eur. Phys. J. D* **67**, 92 (2013).
- [84] B. Friedrich and D. Herschbach, Polarization of molecules induced by intense nonresonant laser fields, *J. Phys. Chem.* **99**, 15686 (1995).
- [85] B. Friedrich, Electro-optical trap for polar molecules, *Phys. Rev. A* **105**, 053126 (2022).
- [86] J. Kongsted and O. Christiansen, Vibrational and thermal effects on the dipole polarizability of methane and carbon tetrachloride from vibrational structure calculations, *J. Chem. Phys.* **127**, 154315 (2007).
- [87] M. Tomza, W. Skomorowski, M. Musiał, R. González-Férez, C. P. Koch, and R. Moszynski, Interatomic potentials, electric properties and spectroscopy of the ground and excited states of the Rb₂ molecule: *ab initio* calculations and effect of a non-resonant field, *Mol. Phys.* **111**, 1781 (2013).
- [88] Q. He, Z. Fang, O. Shoshanim, S. S. Brown, and Y. Rudich, Scattering and absorption cross sections of atmospheric gases in the ultraviolet-visible wavelength range (307–725 nm), *Atmos. Chem. Phys.* **21**, 14927 (2021).
- [89] D. Andrews and A. Demidov, *An Introduction to Laser Spectroscopy* (Springer US, New York City, NY, 2002).
- [90] M. Motsch, M. Zeppenfeld, P. W. H. Pinkse, and G. Rempe, Cavity-enhanced Rayleigh scattering, *New J. Phys.* **12**, 063022 (2010).
- [91] D. W. Sesko, T. G. Walker, and C. E. Wieman, Behavior of neutral atoms in a spontaneous force trap, *J. Opt. Soc. Am. B* **8**, 946 (1991).
- [92] G. Herzberg, *Molecular Spectra and Molecular Structure*, 2nd ed., Prentice-Hall Physics Series (Van Nostrand, New York, 1950).
- [93] C. M. Penney, R. L. S. Peters, and M. Lapp, Absolute rotational Raman cross sections for N₂, O₂, and CO₂, *J. Opt. Soc. Am.* **64**, 712 (1974).
- [94] C. D. Allemand, Depolarization ratio measurements in Raman spectrometry, *Appl. Spectrosc.* **24**, 348 (1970).
- [95] K. Shotton and W. J. Jones, Rotational Raman spectrum of nitric oxide, *Can. J. Phys.* **48**, 632 (1970).
- [96] S. P. S. Porto, Angular dependence and depolarization ratio of the Raman effect, *J. Opt. Soc. Am.* **56**, 1585 (1966).
- [97] W. R. Fenner, H. A. Hyatt, J. M. Kellam, and S. P. S. Porto, Raman cross section of some simple gases, *J. Opt. Soc. Am.* **63**, 73 (1973).
- [98] J. R. Carvalho and L. N. Vidal, Calculation of absolute Raman scattering cross-sections using vibrational self-consistent field/vibrational configuration interaction wave functions, *J. Comput. Chem.* **43**, 1484 (2022).
- [99] L. V. Keldysh, Ionization in the field of a strong electromagnetic wave, *ZhETF* **47**, 1945 (1965) [*Sov. Phys. JETP* **20**, 1307 (1965)].
- [100] S. V. Popruzhenko, V. D. Mur, V. S. Popov, and D. Bauer, Strong Field Ionization Rate for Arbitrary Laser Frequencies, *Phys. Rev. Lett.* **101**, 193003 (2008).

- [101] A. M. Perelomov, V. S. Popov, and M. V. Terent'ev, Ionization of atoms in an alternating electric field, *ZhETF* **50**, 1393 (1966) [*Sov. J. Exp. Theor. Phys.* **23**, 924 (1966)].
- [102] A. L'Huillier, L. A. Lompre, G. Mainfray, and C. Manus, Multiply charged ions induced by multiphoton absorption processes in rare-gas atoms at 1.064 μm , *J. Phys. B* **16**, 1363 (1983).
- [103] M. D. Perry, O. L. Landen, A. Szöke, and E. M. Campbell, Multiphoton ionization of the noble gases by an intense 10^{14} W/cm² dye laser, *Phys. Rev. A* **37**, 747 (1988).
- [104] D. Woodbury, R. M. Schwartz, E. Rockafellow, J. K. Wahlstrand, and H. M. Milchberg, Absolute Measurement of Laser Ionization Yield in Atmospheric Pressure Range Gases over 14 Decades, *Phys. Rev. Lett.* **124**, 013201 (2020).
- [105] S.-F. Zhao, A.-T. Le, C. Jin, X. Wang, and C. D. Lin, Analytical model for calibrating laser intensity in strong-field-ionization experiments, *Phys. Rev. A* **93**, 023413 (2016).
- [106] L.-A. Lompré, A. L'Huillier, G. Mainfray, and C. Manus, Multiphoton ionisation of He atoms at 532 nm, *Phys. Lett. A* **112**, 319 (1985).
- [107] S. L. Chin, Multiphoton ionization of molecules, *Phys. Rev. A* **4**, 992 (1971).
- [108] A. L'Huillier, G. Mainfray, and P. Johnson, Multiphoton ionization versus dissociation of diatomic molecules irradiated by an intense 40 ps laser pulse, *Chem. Phys. Lett.* **103**, 447 (1984).
- [109] A. Hanf, A. Läuter, and H.-R. Volpp, Absolute chlorine atom quantum yield measurements in the UV and VUV gas-phase laser photolysis of CCl₄, *Chem. Phys. Lett.* **368**, 445 (2003).
- [110] A. J. R. Heck, R. N. Zare, and D. W. Chandler, Photofragment imaging of methane, *J. Chem. Phys.* **104**, 4019 (1996).
- [111] H. L. Xu, J. F. Daigle, Q. Luo, and S. L. Chin, Femtosecond laser-induced nonlinear spectroscopy for remote sensing of methane, *Appl. Phys. B* **82**, 655 (2006).
- [112] D. Song, K. Liu, F. Kong, and A. Xia, Neutral dissociation of methane in the ultra-fast laser pulse, *Chin. Sci. Bull.* **53**, 1946 (2008).
- [113] T. E. Carney and T. Baer, The mechanism for multiphoton ionization of H₂ S, *J. Chem. Phys.* **75**, 4422 (1981).
- [114] P. Maitre, D. Scuderi, D. Corinti, B. Chiavarino, M. E. Crestoni, and S. Fornarini, Applications of infrared multiple photon dissociation (IRMPD) to the detection of posttranslational modifications, *Chem. Rev.* **120**, 3261 (2020).
- [115] R. L. Woodin, D. S. Bomse, and J. L. Beauchamp, Multiphoton dissociation of molecules with low power continuous wave infrared laser radiation, *J. Am. Chem. Soc.* **100**, 3248 (1978).
- [116] J. G. Black, E. Yablonovitch, N. Bloembergen, and S. Mukamel, Collisionless Multiphoton Dissociation of SF₆: A Statistical Thermodynamic Process, *Phys. Rev. Lett.* **38**, 1131 (1977).
- [117] R. G. Harrison and S. R. Butcher, Multiple photon infrared processes in polyatomic molecules, *Contemp. Phys.* **21**, 19 (1980).
- [118] N. Bloembergen, C. D. Cantrell, and D. M. Larsen, Collisionless dissociation of polyatomic molecules by multiphoton infrared absorption, in *Tunable Lasers and Applications*, edited by A. Mooradian, T. Jaeger, and P. Stokseth (Springer Berlin Heidelberg, Berlin, Heidelberg, 1976), pp. 162–176.
- [119] N. Bloembergen, I. Burak, and T. B. Simpson, Infrared multiphoton excitation of small molecules, *J. Molecular Struct.* **113**, 69 (1984).
- [120] V. P. Gupta, *Principles and Applications of Quantum Chemistry* (Academic Press, Boston, 2016).
- [121] L. P. Giver, Intensity measurements of the CH₄ bands in the region 4350 Å to 10,600 Å, *J. Quant. Spectrosc. Radiat. Transfer* **19**, 311 (1978).
- [122] D. Rueda, O. V. Boyarkin, T. R. Rizzo, A. Chirokolava, and D. S. Perry, Vibrational overtone spectroscopy of jet-cooled methanol from 5000 to 14000 cm⁻¹, *J. Chem. Phys.* **122**, 044314 (2005).
- [123] N. R. Hutzler, H.-I. Lu, and J. M. Doyle, The buffer gas beam: An intense, cold, and slow source for atoms and molecules, *Chem. Rev.* **112**, 4803 (2012).
- [124] T. Gantner, M. Koller, X. Wu, G. Rempe, and M. Zeppenfeld, Buffer-gas cooling of molecules in the low-density regime: Comparison between simulation and experiment, *J. Phys. B: At. Mol. Opt. Phys.* **53**, 145302 (2020).
- [125] L. Beneventi, P. Casavecchia, and G. G. Volpi, High-resolution total differential cross sections for scattering of helium by O₂, N₂, and NO, *J. Chem. Phys.* **85**, 7011 (1986).
- [126] J. T. Slankas, M. Keil, and A. Kuppermann, Scattering of thermal He beams by crossed atomic and molecular beams. IV. Spherically symmetric intermolecular potentials for He + CH₄, NH₃, H₂O, SF₆, *J. Chem. Phys.* **70**, 1482 (1979).
- [127] Y. S. Au, Inelastic collisions of atomic thorium and molecular thorium monoxide with cold helium-3, Ph.D. thesis, Harvard University, 2013.
- [128] L. Landau and E. Lifshitz, *Statistical Physics* (Elsevier Science, Pergamon Press, Oxford, UK, 2013), Vol. 5.
- [129] R. Bause, A. Schindewolf, R. Tao, M. Duda, X.-Y. Chen, G. Quémener, T. Karman, A. Christianen, I. Bloch, and X.-Y. Luo, Collisions of ultracold molecules in bright and dark optical dipole traps, *Phys. Rev. Res.* **3**, 033013 (2021).
- [130] M. T. Hummon, T. V. Tschersbul, J. Klos, H.-I. Lu, E. Tsikata, W. C. Campbell, A. Dalgarno, and J. M. Doyle, Cold N+NH Collisions in a Magnetic Trap, *Phys. Rev. Lett.* **106**, 053201 (2011).
- [131] J. G. E. Harris, R. A. Michniak, S. V. Nguyen, N. Brahm, W. Ketterle, and J. M. Doyle, Buffer gas cooling and trapping of atoms with small effective magnetic moments, *Europhys. Lett.* **67**, 198 (2004).
- [132] R. Michniak, Enhanced buffer gas loading: Cooling and trapping of atoms with low effective magnetic moments, Ph.D. thesis, Harvard University, 2004.
- [133] W. Ketterle and N. V. Druten, Evaporative cooling of trapped atoms, in *Advances In Atomic, Molecular, and Optical Physics*, Vol. 37, edited by B. Bederson and H. Walther (Academic Press, Cambridge, MA, 1996), pp. 181–236.
- [134] R. Bourgain, J. Pellegrino, A. Fuhrmanek, Y. R. P. Sortais, and A. Browaeys, Evaporative cooling of a small number of atoms in a single-beam microscopic dipole trap, *Phys. Rev. A* **88**, 023428 (2013).
- [135] K. M. O'Hara, M. E. Gehm, S. R. Granade, and J. E. Thomas, Scaling laws for evaporative cooling in time-dependent optical traps, *Phys. Rev. A* **64**, 051403(R) (2001).
- [136] S. K. Lee, J. J. Kim, and D. Cho, Transformable optical dipole trap using a phase-modulated standing wave, *Phys. Rev. A* **74**, 063401 (2006).

- [137] P. D. Edmunds and P. F. Barker, Trapping Cold Ground State Argon Atoms, *Phys. Rev. Lett.* **113**, 183001 (2014).
- [138] U. Boesl and R. Zimmermann, Fundamentals and Mechanisms of Resonance-Enhanced Multiphoton Ionization (REMPI) in Vacuum and its Application in Molecular Spectroscopy, in *Photoionization and Photo-Induced Processes in Mass Spectrometry* (John Wiley & Sons, Ltd, 2021), Chap. 2, pp. 23–88.
- [139] H. Yamaguchi, T. Moriyama, K. Ide, J. Ito, Y. Matsuda, and T. Niimi, Measurement of the rotational temperature in a nitrogen molecular beam by REMPI, *AIP Conf. Proc.* **1501**, 1350 (2012).
- [140] M. Ashfold and C. Western, Multiphoton spectroscopy, applications, in *Encyclopedia of Spectroscopy and Spectrometry*, edited by J. C. Lindon, G. E. Tranter, and D. W. Koppenaal, 3rd ed. (Academic Press, Oxford, 2017), pp. 954–961.
- [141] M. Nolde, K.-M. Weitzel and C. M. Western, The resonance enhanced multiphoton ionisation spectroscopy of ammonia isotopomers NH_3 , NH_2D , NHD_2 , and ND_3 , *Phys. Chem. Chem. Phys.* **7**, 1527 (2005).
- [142] P. M. Johnson, The multiphoton ionization spectrum of benzene, *J. Chem. Phys.* **64**, 4143 (1976).
- [143] B. Xue, Y. Chen, and H.-L. Dai, Observation of the singlet-triplet pair of the 4p Rydberg state and assignment of the Rydberg series of SO_2 , *J. Chem. Phys.* **112**, 2210 (2000).
- [144] G. Meijer, J. J. ter Meulen, P. Andresen, and A. Bath, Sensitive quantum state selective detection of H_2O and D_2O by (2+1)-resonance enhanced multiphoton ionization, *J. Chem. Phys.* **85**, 6914 (1986).
- [145] J. G. Philis, Resonance-enhanced multiphoton ionization spectra of jet-cooled methanol and ethanol, *Chem. Phys. Lett.* **449**, 291 (2007).
- [146] A. Dogariu, C. Stein, A. Glaser, and R. B. Miles, Long range trace detection by radar REMPI, in *Advanced Environmental, Chemical, and Biological Sensing Technologies VIII*, Vol. 8024, edited by T. Vo-Dinh, R. A. Lieberman, and G. Gauglitz, *International Society for Optics and Photonics* (SPIE, Orlando, FL, 2011), pp. 88–96.
- [147] E. de Beer, M. P. Koopmans, C. A. de Lange, Y. Wang, and W. A. Chupka, (2+1) resonance-enhanced multiphoton ionization-photoelectron spectroscopy of the OH radical, *J. Chem. Phys.* **94**, 7634 (1991).
- [148] T. Streibel and R. Zimmermann, Resonance-enhanced multiphoton ionization mass spectrometry (REMPI-MS): Applications for process analysis, *Annu. Rev. Anal. Chem.* **7**, 361 (2014).
- [149] Z. Zhang, M. N. Shneider, and R. B. Miles, Coherent microwave scattering from resonance enhanced multi-photon ionization (radar REMPI): a review, *Plasma Sources Sci. Technol.* **30**, 103001 (2021).
- [150] S. A. Levshakov, M. G. Kozlov, and D. Reimers, Methanol as a tracer of fundamental constants, *Astrophys. J.* **738**, 26 (2011).
- [151] T. Yang, L. Huang, C. Xiao, J. Chen, T. Wang, D. Dai, F. Lique, M. H. Alexander, Z. Sun, D. H. Zhang, X. Yang, and D. M. Neumark, Enhanced reactivity of fluorine with *para*-hydrogen in cold interstellar clouds by resonance-induced quantum tunnelling, *Nat. Chem.* **11**, 744 (2019).
- [152] R. J. Shannon, M. A. Blitz, A. Goddard, and D. E. Heard, Accelerated chemistry in the reaction between the hydroxyl radical and methanol at interstellar temperatures facilitated by tunnelling, *Nat. Chem.* **5**, 745 (2013).
- [153] A. Christianen, T. Karman, and G. C. Groenenboom, Quasi-classical method for calculating the density of states of ultracold collision complexes, *Phys. Rev. A* **100**, 032708 (2019).
- [154] L. E. Snyder, F. J. Lovas, J. M. Hollis, D. N. Friedel, P. R. Jewell, A. Remijan, V. V. Ilyushin, E. A. Alekseev, and S. F. Dyubko, A rigorous attempt to verify interstellar glycine, *Astrophys. J.* **619**, 914 (2005).
- [155] J. Tennyson, Perspective: Accurate ro-vibrational calculations on small molecules, *J. Chem. Phys.* **145**, 120901 (2016).
- [156] A. Beyer, L. Maisenbacher, A. Matveev, R. Pohl, K. Khabarova, A. Grinin, T. Lamour, D. C. Yost, T. W. Hänsch, N. Kolachevsky, and T. Udem, The Rydberg constant and proton size from atomic hydrogen, *Science* **358**, 79 (2017).
- [157] A. Grinin, A. Matveev, D. C. Yost, L. Maisenbacher, V. Wirthl, R. Pohl, T. W. Hänsch, and T. Udem, Two-photon frequency comb spectroscopy of atomic hydrogen, *Science* **370**, 1061 (2020).
- [158] J. Ye, H. J. Kimble, and H. Katori, Quantum state engineering and precision metrology using state-insensitive light traps, *Science* **320**, 1734 (2008).
- [159] S. S. Kondov, C.-H. Lee, K. H. Leung, C. Liedl, I. Majewska, R. Moszynski, and T. Zelevinsky, Molecular lattice clock with long vibrational coherence, *Nat. Phys.* **15**, 1118 (2019).
- [160] K. H. Leung, B. Iritani, E. Tiberi, I. Majewska, M. Borkowski, R. Moszynski, and T. Zelevinsky, Terahertz Vibrational Molecular Clock with Systematic Uncertainty at the 10^{-14} Level, *Phys. Rev. X* **13**, 011047 (2023).
- [161] H. Jóźwiak and P. Wcisło, Magic wavelength for a rovibrational transition in molecular hydrogen, *Sci. Rep.* **12**, 14529 (2022).
- [162] R. Boyd, *Nonlinear Optics*, 4th ed. (Academic Press, London, 2020).
- [163] M. Abramowitz and I. A. Stegun, *Handbook of Mathematical Functions, with Formulas, Graphs, and Mathematical Tables*, Dover Books on Intermediate and Advanced Mathematics (Dover Publications, New York, 1964).
- [164] P. Virtanen, R. Gommers, T. E. Oliphant, M. Haberland, T. Reddy, D. Cournapeau, E. Burovski, P. Peterson, W. Weckesser, J. Bright, S. J. van der Walt, M. Brett, J. Wilson, K. J. Millman, N. Mayorov, A. R. J. Nelson, E. Jones, R. Kern, E. Larson, C. J. Carey *et al.*, SciPy 1.0: fundamental algorithms for scientific computing in Python, *Nat. Methods* **17**, 261 (2020).
- [165] E. F. Archibong and A. J. Thakkar, Static hyperpolarizability of N_2 , *J. Chem. Phys.* **100**, 7471 (1994).
- [166] Y. Luo, H. Ågren, B. Minaev, and P. Jørgensen, The hyperpolarizability of molecular oxygen, *J. Mol. Struct. (THEOCHEM)* **336**, 61 (1995).
- [167] G. Maroulis, Electric polarizability and hyperpolarizability of carbon monoxide, *J. Phys. Chem.* **100**, 13466 (1996).
- [168] B. Fernández, S. Coriani, and A. Rizzo, MCSCF polarizability and hyperpolarizabilities of HCl and HBr, *Chem. Phys. Lett.* **288**, 677 (1998).
- [169] R. N. Fernandez and D. P. Shelton, Hyperpolarizability dispersion measured for CS_2 vapor, *J. Opt. Soc. Am. B* **37**, 1769 (2020).

- [170] G. Maroulis and A. J. Thakkar, Multipole moments, polarizabilities, and hyperpolarizabilities for N_2 from fourth-order many-body perturbation theory calculations, *J. Chem. Phys.* **88**, 7623 (1988).
- [171] H. Davies, The reflection of electromagnetic waves from a rough surface, *Proc. IEE - Part IV: Institution Monographs* **101**, 209 (1954).
- [172] H. E. Bennett and J. O. Porteus, Relation between surface roughness and specular reflectance at normal incidence, *J. Opt. Soc. Am.* **51**, 123 (1961).
- [173] A. Steyerl, S. Malik, and L. Iyengar, Specular and diffuse reflection and refraction at surfaces, *Phys. B: Condens. Matter* **173**, 47 (1991).
- [174] T. A. Savard, K. M. O'Hara, and J. E. Thomas, Laser-noise-induced heating in far-off resonance optical traps, *Phys. Rev. A* **56**, R1095 (1997).
- [175] C. W. Gardiner, J. Ye, H. C. Nagerl, and H. J. Kimble, Evaluation of heating effects on atoms trapped in an optical trap, *Phys. Rev. A* **61**, 045801 (2000).
- [176] A. Christianen, M. W. Zwierlein, G. C. Groenenboom, and T. Karman, Photoinduced Two-Body Loss of Ultracold Molecules, *Phys. Rev. Lett.* **123**, 123402 (2019).
- [177] R. Hellmann, E. Bich, and E. Vogel, *Ab initio* intermolecular potential energy surface and second pressure virial coefficients of methane, *J. Chem. Phys.* **128**, 214303 (2008).
- [178] R. Hellmann, *Ab initio* potential energy surface for the nitrogen molecule pair and thermophysical properties of nitrogen gas, *Mol. Phys.* **111**, 387 (2013).
- [179] S. Ospelkaus, K. Ni, D. Wang, M. H. G. de Miranda, B. Neyenhuis, G. Quémener, P. S. Julienne, J. L. Bohn, D. S. Jin, and J. Ye, Quantum-state controlled chemical reactions of ultracold potassium-rubidium molecules, *Science* **327**, 853 (2010).
- [180] P. S. Julienne, Ultracold molecules from ultracold atoms: a case study with the KRb molecule, *Faraday Discuss.* **142**, 361 (2009).
- [181] J. Tao and A. M. Rappe, Communication: Accurate higher-order van der Waals coefficients between molecules from a model dynamic multipole polarizability, *J. Chem. Phys.* **144**, 031102 (2016).
- [182] L. Frommhold, *Collision-induced Absorption in Gases*, Cambridge Monographs on Atomic, Molecular and Chemical Physics (Cambridge University Press, Cambridge, UK, 1994).
- [183] T. Karman, M. A. J. Koenis, A. Banerjee, D. H. Parker, I. E. Gordon, A. van der Avoird, W. J. van der Zande, and G. C. Groenenboom, O_2 - O_2 and O_2 - N_2 collision-induced absorption mechanisms unravelled, *Nat. Chem.* **10**, 549 (2018).
- [184] A. E. Belikov and R. G. Sharafutdinov, Rotational relaxation time in free jets of He + N_2 mixtures, *Chem. Phys. Lett.* **241**, 209 (1995).
- [185] D. R. Miller and R. P. Andres, Rotational relaxation of molecular nitrogen, *J. Chem. Phys.* **46**, 3418 (1967).
- [186] A. E. Belikov, I. Y. Solov'ev, G. I. Sukhinin, and R. G. Sharafutdinov, Rotational relaxation time of nitrogen, *J. Appl. Mech. Tech. Phys.* **29**, 630 (1988).
- [187] C. G. Morgan, Laser-induced breakdown of gases, *Rep. Prog. Phys.* **38**, 621 (1975).
- [188] A. Ali, *On Laser Air Breakdown, Threshold Power and Laser Generated Channel Length*, Tech. Rep. No. ADA133211 (Naval Research Lab, Washington, DC, 1983).
- [189] D. I. Rosen and G. Weyl, Laser-induced breakdown in nitrogen and the rare gases at 0.53 and 0.357 μm , *J. Phys. D* **20**, 1264 (1987).
- [190] L. J. Radziemski and D. A. Cremers, *Laser-Induced Plasmas and Applications*, Optical engineering: Vol. 21 (CRC Press, Boca Raton, FL, 1989).
- [191] J. Isaacs, C. Miao, and P. Sprangle, Remote monostatic detection of radioactive material by laser-induced breakdown, *Phys. Plasmas* **23**, 033507 (2016).
- [192] H. Brehme, Laser-induced multiphoton processes in e^- - p scattering, *Phys. Rev. C* **3**, 837 (1971).
- [193] J. F. Seely and E. G. Harris, Heating of a plasma by multiphoton inverse bremsstrahlung, *Phys. Rev. A* **7**, 1064 (1973).
- [194] P. Cavaliere, G. Ferrante, and C. Leone, Particle-atom ionising collisions in the presence of a laser radiation field, *J. Phys. B* **13**, 4495 (1980).
- [195] M. Zarcone, D. L. Moores, and M. R. C. McDowell, Laser-assisted electron impact ionisation of helium at 256.5 eV, *J. Phys. B* **16**, L11 (1983).
- [196] M. J. Brunger, S. J. Buckman, L. J. Allen, I. E. McCarthy, and K. Ratnavelu, Elastic electron scattering from helium: Absolute experimental cross sections, theory and derived interaction potentials, *J. Phys. B* **25**, 1823 (1992).
- [197] Y. Ralchenko, R. K. Janev, T. Kato, D. V. Fursa, I. Bray, and F. de Heer, *Cross Section Database for Collision Processes of Helium Atom with Charged Particles. I. Electron impact processes*, Tech. Rep. No. NIFS-DATA-59 (NIFS, Japan, 2000).
- [198] R. G. Montague, M. F. A. Harrison, and A. C. H. Smith, A measurement of the cross section for ionisation of helium by electron impact using a fast crossed beam technique, *J. Phys. B* **17**, 3295 (1984).
- [199] M.-Y. Song, J.-S. Yoon, H. Cho, Y. Itikawa, G. P. Karwasz, V. Kokoouline, Y. Nakamura, and J. Tennyson, Cross sections for electron collisions with methane, *J. Phys. Chem. Ref. Data* **44**, 023101 (2015).
- [200] M. C. Fuss, A. Muñoz, J. C. Oller, F. Blanco, M.-J. Hubin-Franskin, D. Almeida, P. Limão-Vieira, and G. García, Electronmethane interaction model for the energy range 0.1–10000 eV, *Chem. Phys. Lett.* **486**, 110 (2010).
- [201] Y.-K. Kim, W. R. Johnson, and M. E. Rudd, Cross sections for singly differential and total ionization of helium by electron impact, *Phys. Rev. A* **61**, 034702 (2000).
- [202] W. Hwang, Y. Kim, and M. E. Rudd, New model for electron-impact ionization cross sections of molecules, *J. Chem. Phys.* **104**, 2956 (1996).
- [203] Y. Itikawa, Cross sections for electron collisions with nitrogen molecules, *J. Phys. Chem. Ref. Data* **35**, 31 (2006).
- [204] Y. Itikawa, Cross sections for electron collisions with oxygen molecules, *J. Phys. Chem. Ref. Data* **38**, 1 (2009).